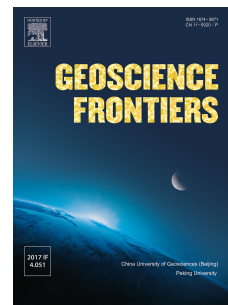


Journal Pre-proof

Dating long thrust systems on Mercury: new clues on the thermal evolution of the planet

L. Giacomini, M. Massironi, V. Galluzzi, S. Ferrari, P. Palumbo



PII: S1674-9871(19)30169-0

DOI: <https://doi.org/10.1016/j.gsf.2019.09.005>

Reference: GSF 886

To appear in: *Geoscience Frontiers*

Received Date: 28 February 2019

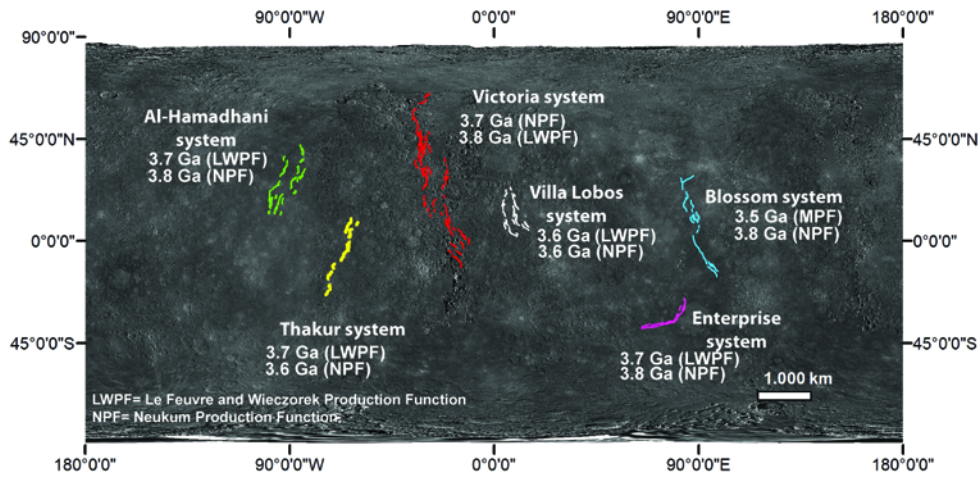
Revised Date: 16 July 2019

Accepted Date: 25 September 2019

Please cite this article as: Giacomini, L., Massironi, M., Galluzzi, V., Ferrari, S., Palumbo, P., Dating long thrust systems on Mercury: new clues on the thermal evolution of the planet, *Geoscience Frontiers*, <https://doi.org/10.1016/j.gsf.2019.09.005>.

This is a PDF file of an article that has undergone enhancements after acceptance, such as the addition of a cover page and metadata, and formatting for readability, but it is not yet the definitive version of record. This version will undergo additional copyediting, typesetting and review before it is published in its final form, but we are providing this version to give early visibility of the article. Please note that, during the production process, errors may be discovered which could affect the content, and all legal disclaimers that apply to the journal pertain.

© 2019 China University of Geosciences (Beijing) and Peking University. Production and hosting by Elsevier B.V. All rights reserved.



1 **Dating long thrust systems on Mercury: new clues on the thermal evolution of the planet.**

2 L. Giacomini ^{a,*}, M. Massironi ^b, V. Galluzzi ^a, S. Ferrari ^c, P. Palumbo ^d

3 ^a INAF-IAPS, Istituto di Astrofisica e Planetologia Spaziali, via Fosso del Cavaliere 100, 00133 Roma, Italy.

4 ^b Dipartimento di Geoscienze, University of Padova, via G. Gradenigo 6, 35131 Padova, Italy

5 ^c Center of Studies and Activities for Space (CISAS) “G. Colombo”, University of Padova, Via Venezia 15,
6 35131 Padova, Italy.

7 ^d Dipartimento di Scienze e Tecnologie, University of Naples “Parthenope”, Centro Direzionale, Isola C4,
8 80143 Napoli, Italy.

9 *Corresponding author. E-mail: lorenza.giacomini@inaf.it

10

11 Abstract

12 The global tectonics of Mercury is dominated by contractional features mainly represented by
13 lobate scarps, high relief ridges, and wrinkle ridges. These structures are the expression of thrust
14 faults and are linear or arcuate features widely distributed on Mercury. Locally, these structures are
15 arranged in long systems characterized by a preferential orientation and non-random spatial
16 distribution. In this work we identified five thrust systems, generally longer than 1000 km. They
17 were named after the main structure or crater encompassed by the system as: Thakur, Victoria, Villa
18 Lobos, Al-Hamadhani, and Enterprise. In order to gain clues about their formation, we dated them
19 using the buffered crater counting technique, which can be applied to derive the ages of linear
20 landforms such as faults, ridges and channels. To estimate the absolute age for the end of the thrust
21 system’s activity, we applied both Le Feuvre and Wieczorek Production Function and Neukum
22 Production Functions. Moreover, to further confirm the results obtained with the buffered crater
23 counting method, the classic stratigraphic approach has been adopted, in which a faulted and an
24 unfaulted craters were dated for each system. The results gave consistent ages and suggested that
25 the most movements along major structures all over Mercury most likely ended at about 3.6–3.8 Ga.
26 This gives new clues to better understand the tectonics of the planet and, therefore, its thermal
27 evolution. Indeed, the early occurrence of tectonic activity in the planet’s history, well before than
28 predicted by the thermophysical models, coupled with the orientation and spatial distribution of the
29 thrust systems, suggests that other processes beside global contraction, like mantle downwelling or
30 tidal despinning, could have contributed to the first stage of the planet’s history.

31

32 **Keywords:** Mercury; thrust systems; crater counting; thermal evolution; planetary geology;
33 structural geology

34

35 1. Introduction

36

37 When the NASA Mariner 10 spacecraft approached Mercury in 1974, it revealed a planet with
38 widespread tectonic landforms on its surface. About forty years later, this was further confirmed by
39 the NASA MESSENGER (MErcury Surface, Space ENvironment, GEochemistry and Ranging)
40 mission that performed global mapping of the planet, revealing that Mercury's tectonic fabric is
41 widely distributed on the entire surface.

42 The observed tectonic features are mainly represented by structures named lobate scarps, high relief
43 ridges, and wrinkle ridges, which are different expressions of compressive stress acting on the
44 surface (Strom et al., 1975).

45 In particular, lobate scarps are surface expression of thrust faults, linear or arcuate in plan view.
46 They are generally asymmetric in cross section with a steeply sloping scarp face and a gently
47 sloping back limb (e.g. Watters et al., 2015), probably representing a monocline or asymmetric
48 hanging-wall anticline atop a blind or surface-breaking thrust fault (Byrne et al., 2014; Massironi et
49 al., 2015). High relief ridges are less common than lobate scarps and more symmetric in cross
50 section (e.g. Dzurisin, 1978). These features exhibit both horizontal shortening and vertical offset of
51 the wall. Finally, wrinkle ridges are broad, low-relief arches with a narrow superposed ridge. They
52 are interpreted to be the result of a combination of folding and faulting, i.e. an anticlinal fold above
53 a blind thrust fault (Byrne et al., 2014; Watters et al., 2015 and references therein).

54 The global distribution of these contractional features led several authors to hypothesize that they
55 could be the expression of two major processes: global contraction (Watters et al., 1998, 2009a;
56 Watters and Nimmo, 2010), tidal despinning (Burns, 1976; Melosh and Dzurisin, 1978; Melosh,
57 1997; Melosh and McKinnon, 1998), or a combination of the two (Pechmann and Melosh, 1979;
58 Dombard and Hauck, 2008; Matsuyama and Nimmo, 2009; Beuthe, 2010; Klimczak et al., 2015).
59 More recently, mantle convection has also been invoked as a possible mechanism (King 2008;
60 Michel et al., 2013; Massironi et al., 2015).

61 Global contraction results from the progressive cooling of planet's interior. The decrease of the
62 internal temperature causes phase changes such as those associated with the solidification of the
63 inner core (e.g. Solomon 1976, 1977; Schubert et al., 1988; Hauck et al., 2004; Grott et al., 2011). If
64 global contraction acted alone, it should have caused global, horizontally isotropic compressional
65 stresses and a uniformly distributed population of randomly oriented lobate scarps (Klimczak et al.,
66 2015; Watters et al., 2015).

67 Tidal despinning, instead, is the slowing of an initially rapid rotation accompanied by a relaxation
68 of the equatorial tidal bulge. Initially, this process was thought to cause a distinctive latitude-
69 dependent pattern with an equatorial zone of N-S oriented thrust faults, a middle-latitude zone
70 characterized by strike-slip faults with a NE-SW and NW-SE orientations, and, finally, polar
71 regions with E-W oriented normal faults (Melosh, 1978). Recently, however, Klimczak et al.
72 (2015) took into account the elastic properties of lithosphere and concluded that tidal despinning
73 alone would only produce a global set of opening-mode fractures with no preferred orientation at
74 the poles, with progressively preferred east-west orientation towards the equator.

75 Neither global contraction nor tidal despinning, however, fits with the observed global pattern of
76 Mercury, which shows a prevalent N-S orientated thrust faults on the equatorial areas and a slight
77 E-W orientated thrust faults at the higher latitudes (Watters et al., 2015). If global contraction and

78 tidal despinning operated simultaneously for a certain time span, the resulting fabric would include
79 N–S oriented thrusts at the equator and middle latitude and randomly oriented thrusts at the poles
80 (Klimczak et al., 2015).

81 Alternatively, mantle convection suggests that compressional stresses along zones of mantle
82 downwelling would enhance the localization of N–S oriented faults at lower latitude and E–W
83 faults at higher latitude (King, 2008, Michel et al., 2013).

84 Improved knowledge of the duration and timing of these processes could help to understand which
85 mechanism – or combination of mechanism – is responsible for the formation of the observed
86 pattern of tectonic structures on Mercury. To this end, we identified several long thrust systems,
87 distributed over the planet's surface (Fig. 1), and we determined their ages, not only through
88 stratigraphic relationships, but also with the absolute model age assessments through crater size-
89 frequency distribution (CSFD) measurements and using the Buffered Crater Counting (BCC)
90 technique.

91

92

93 2. Data and Methods

94

95 The first phase of this work was to identify the thrust systems, searching for a series of clustered
96 thrust segments, linked together at the surface and characterized by a consistent trend and vergence.
97 Based on this, we can state that these thrusts formed in response to the same forces. Since our aim is
98 to study the stress regime acting on the planet surface at a regional scale, we considered systems
99 with a considerable length, generally exceeding 1000 km. In addition, this allows collecting a
100 significant number of craters, obtaining a good statistic from the crater counting.

101 A change of vergence with respect to the main structures can be locally observed in correspondence
102 of craters. This can be due to pre-existing anisotropies potentially related to the craters themselves,
103 causing the formation of faults with an opposite vergence. Thrusts showing coherent orientation but
104 an opposite vergence with respect to the primary faults, and that do not represent back-thrusts of the
105 main structures or are not related to preexisting craters, were not included in the systems. Moreover,
106 we did not take into account wrinkle ridges located in the widespread smooth plains of the northern
107 latitudes and Caloris basin surroundings (Denevi et al., 2013), since they could have been
108 developed in response also of loading-induced stresses, which depend by the thickness and
109 distribution of smooth plain material (Watters et al., 2009b).

110 To identify these systems we used the MESSENGER MDIS (Mercury Dual Imaging System)
111 monochrome global mosaic with a spatial resolution of 250 m/pixel compiled using NAC (Narrow
112 Angle Camera) and WAC (Wide Angle Camera) images acquired in the filter centered at 750 nm
113 (Fig. 1).

114 Once the systems were detected, we used the MDIS map projected basemap reduced data record
115 (BDR) monochrome mosaics with a higher spatial resolution of 166 m/pixel as basemap to outline

116 each specific thrust system. The BDR mosaic is made of NAC and WAC 750-nm images
117 illuminated with a solar incidence angle around 74° . The basemap mosaics illuminated with high
118 solar incidence angle both from east (HIE) and west (HIW) were also considered to better
119 distinguish the structures. For each thrust system the mosaics were processed with USGS Integrated
120 Software for Imagers and Spectrometers (ISIS) and reprojected with ArcGIS in order to center them
121 at the latitude and longitude of the feature. This procedure was performed to avoid distortion and
122 the consequent alteration of the final length of the fault systems. Finally, the tectonic structures
123 were digitized as vector shapefiles.

124 2.1 The buffered crater counting technique (BCC) and the stratigraphic method

125 To date the thrust systems we used the BCC technique, a method developed by Tanaka (1982) to
126 derive the age of linear features (such as faults and channels) and subsequently employed by
127 Wichman and Schultz (1989) to study large-scale Martian extensional tectonics. More recently, this
128 technique has been used by Fassett and Head (2008), Hoke and Hynes (2009), and Bouley et al.
129 (2010) to determine the age of Martian valley networks, and by Kneissl et al. (2015) to date Martian
130 graben systems. Giacomini et al. (2015) and Galluzzi et al. (2016a, 2019), applied the method on
131 Mercury to date the Blossom and Victoria thrust systems, respectively, whereas Fegan et al. (2017)
132 dated some Hermean basin-edge lobate scarps. Finally, this technique has also been used on lunar
133 wrinkle ridges (Clark et al., 2017; Yue et al., 2017), and lobate scarps (Senthil Kumar et al., 2016;
134 van der Bogert et al., 2018)

135 The BCC method assumes that it is possible to determine a stratigraphic relationship between
136 lineaments and craters. Indeed, only craters formed after the lineaments can be considered in the
137 count to date the end of thrust systems' activity. To estimate such a stratigraphic relationship, two
138 different approaches can be followed. The broadest one considers all the craters superposed on the
139 structures as well as those whose ejecta lay over the lineaments. In this latter case, craters located at
140 a certain distance from the lineaments are also considered in the count. This allows more craters to
141 be considered. However, quite often it is not easy to discern whether the crater ejecta superimpose a
142 lineament or not, with a consequent greater uncertainty in the age estimation. The second approach
143 is more stringent and considers only those craters whose rim intersects the lineaments.

144 In this work, we adopted the latter approach in order to be more confident that the counted craters
145 are formed after the structures.

146 To perform the BCC, the "CraterTool" software developed by Kneissl et al. (2011) was employed.
147 This application automatically calculates the required buffer width for each crater and creates buffer
148 polygons around the linear features, merging the overlapping areas.

149 With the CraterTool software the width of the buffer can be chosen from 1R to 3R (R= radius of
150 crater), depending on which approach has been adopted. In the case of 1R, no crater ejecta are taken
151 into account. On the contrary, in the case of 2R and 3R, the extensions of crater's ejecta of two or
152 three radii (from the center of the crater) are considered, respectively.

153 In this work, although during the selection of craters we adopted the more stringent method (i.e.
154 only craters whose rim overlays the structures), we considered also the ejecta of the craters to
155 estimate the buffer areas. Indeed, we assumed that every crater formed its ejecta during the impact;
156 therefore we held that they should be included in the estimate of the buffered areas. Hence, we
157 chose a buffer width equal to 2R. Actually, Melosh (1989) states that crater ejecta can extend up to

158 one diameter from the crater rim (i.e. 3R from the crater center) but, according to Gault et al.(1975),
159 the ejecta on Mercury extent up to 2R from the center of the crater.

160 Therefore, the buffered area (A) can be expressed as:

161

162

$$163 \quad A = 2(S_{\text{buffer}}) \times L$$

164

165 Where L is the length of the structure and S_{buffer} is:

166

$$167 \quad S_{\text{buffer}} = 2R + 0.5W$$

168

169 W being the width of the linear feature that is mapped as an elongated polygon. Such polygon needs
170 to include surfaces formed during the same event. Therefore, to draw it, we considered as thrust
171 width just the thrust's scarp, where we are more confident that preexisting craters were erased. On
172 the contrary, if we include in this polygon also thrust-related landforms (e.g. anticlinal folds
173 associated with thrusts), we cannot assure that all of the craters located within these areas
174 effectively postdate the thrust, since some preexisting craters could have persisted. Consequently,
175 also some craters predating the structures could be counted, with the overestimation of the system's
176 age.

177 In this work the width for all the structures was considered as 2 km, which is the minimum width
178 that includes the thrust's scarps. We performed also some tests considering a width of 1 km and 4
179 km but no significant changes in the final results were obtained.

180 To be more conservative, we decided to consider also the case where no crater ejecta have been
181 taken into account ($S_{\text{buffer}} = R + 0.5W$), in order to compare the results obtained considering the two
182 different approaches on calculating the buffer areas.

183 Since the thrust systems under study are considerably long, geodesic buffers were applied in order
184 to avoid projection distortions and consequent erroneous calculations of buffered areas. Indeed, the
185 geodesic buffer takes into account the curvature of the planet's surface, giving more accurate buffer
186 offsets and, therefore, more precise buffered areas, in particular for features that cover long
187 distances in latitude.

188 As highlighted in previous works (Wichman and Schultz 1989; Fassett and Head 2008; Bouley et
189 al. 2010), one of the most important constraints of the BCC method is the limited number of crater
190 statistics for small features. However, as all the considered systems are quite long (from 800 km to
191 3500 km), the counts involved a large area and the crater count-derived statistics can be considered
192 robust. Recently, BCC technique was also applied on small scarps on the Moon (van der Bogert et
193 al., 2018). Despite the modest lengths, BCC results show generally a good agreement with the
194 traditional CSFD measurement (van der Bogert et al., 2018), suggesting that the technique is
195 efficient on dating also small features, if a sufficient superposing craters are collected. This was
196 allowed by the high resolution of the satellite images available for the lunar surface (e.g. up to 0.50
197 m/pixel for LROC images), which permitted to obtain, in most of the cases, a solid statistic.

198 After the buffer crater counts, the resulting crater size-frequency data were exported with the
199 CraterTools software in a format compatible with the Craterstats analysis software (Michael and
200 Neukum, 2010) used to determine absolute model ages for the thrust systems. Craterstats allows an
201 estimation of the age by performing a best fit of the CSFD and then providing the absolute model

202 age value with the relative errors (based on the statistics of Poisson cratering process related to the
203 nonlinear chronology functions of the models; Michael and Neukum, 2010). The best fit was
204 performed considering craters diameters larger than 2–3 km, and minimizing the relative errors. The
205 smaller craters were avoided since a progressive fall-off is observed, which is likely due to the
206 resolution limit of used images (Michael and Neukum, 2010). Moreover, considering small craters
207 can lead to the inclusion of secondaries. The contribution of secondary craters within the smaller
208 diameter ranges (< 10 km on Mercury; e.g. Strom et al., 2011) is still a matter of debate. Indeed, for
209 some authors secondary craters dominate the small crater population, whereas, according to other
210 authors, secondaries are negligible or, at least, they are integrated in the crater chronology, so their
211 contribution has already been included in the crater statistics (Xiao et al., 2018 and reference
212 therein). In order to avoid as much as possible the influence of secondaries, we excluded from our
213 counts all the craters that are arranged in clusters or chains and that show an irregular rim or shape,
214 signs of low energy impacts, which are likely the results of secondary impacts (Melosh, 1989).
215 Finally, we also performed a more classic stratigraphic dating, in order to validate the results of the
216 BCC method. For each system, one crater that has been cut by thrusts and one crater that superposes
217 the thrusts were dated. This allows a maximum and a minimum age limit of the thrust activity to be
218 obtained, respectively. To gain the narrowest time range for the thrust system activity, we should
219 date the youngest among the faulted craters and the oldest among the unfaulted craters. To reach this
220 aim it is preferable to choose a faulted crater showing a less cratered floor (for the maximum limit)
221 and an unfaulted crater showing a more cratered floor (for the minimum limit). However, this is not
222 always possible since we had to avoid craters affected by secondaries of subsequent craters that
223 could invalidate the statistics. Consequently, often the time gap between the age obtained with the
224 BCC method and maximum and minimum age limits is very wide. This implies that the chosen
225 faulted craters can be formed considerably before the thrust occurrence and, on the contrary, that
226 unfaulted craters could be emplaced well after the end of thrust system activity. Although maximum
227 and minimum limits obtained with the stratigraphic method do not reflect the effective age of the
228 systems' activity, they provide a time range that can be used to test the BCC technique, since the
229 results of the two different approaches need to be concordant.

230 In several cases, the chosen craters have a limited area, thus, to date them we employed single
231 MDIS images at higher resolution, which have been calibrated and georeferenced with ISIS
232 software.

233 A limited area also implies that often the CSFD mainly includes small diameters, less than 10 km,
234 implying that possible far field secondaries can contribute to the crater population. In order to
235 minimize their contribution we consider, for the stratigraphic study, craters that are far from the
236 largest basins, whose secondary craters could have affected the surrounding areas. Nevertheless,
237 during the count, craters with irregular morphologies and/or arranged in chains and clusters have
238 been excluded and areas occupied by them were clipped and removed from the counting area (Platz
239 et al., 2013).

240 Regarding the minimum age limit, in some cases the considered craters are very young (i.e. the case
241 of Thakur and Enterprise thrust system). Although the diameters considered in the count have
242 diameters < 1 km, we can be confident that the CSFDs are not affected by secondaries since the
243 craters emplaced after the LHB, when the formation of large craters was rarer, and the contribution
244 of far field secondary impact craters is less significant (Strom et al., 2011).

245 In fact, the CSFDs resulting from the counts do not show an evident steepening for small diameters,
246 suggesting that the effects of secondaries are negligible.

247

248

249 2.2 Crater chronology models

250

251 To obtain an absolute model age of both the lineaments and the crater floors we used two different
 252 models: the model Production Function proposed by Le Feuvre and Wieczorek (hereafter called
 253 LWPF) (Le Feuvre and Wieczorek, 2011) and the Neukum Production Function (NPF) (Neukum et
 254 al., 2001a).

255 Neukum et al. (2001a) derived the Mercurian Production Function from the lunar Neukum
 256 Production Function (Neukum, 1983; Neukum and Ivanov 1994; Neukum et al. 2001a, b), by
 257 applying a scaling law relative to the impactor flux and its velocity distribution, and by taking into
 258 account the differences in gravitational acceleration and target properties (Hartmann 1977; Strom
 259 and Neukum 1988; Neukum et al. 2001a, b). Since NPF was the most known and used
 260 chronological model in the past, we decided to use also this model to give a basis of comparison
 261 with the ages previously calculated for Mercurian features.

262 LWPF is a more recent model that takes into account the impactor flux that affected the planet
 263 surface as well as the different rheological proprieties of the surface itself.

264 It assumes that the impactor SFD is the same for all the planets and the impact probability is
 265 independent of the projectile size. To derive the CSFD from the impactor SFD Le Feuvre and
 266 Wieczorek (2011) used the porous scaling law and the non-porous scaling law of Holsapple and
 267 Housen (2007), based on the target rheology. In the LWPF only the gravity regime is considered on
 268 the scaling law and therefore tensile strengths of rocks are negligible (this holds for crater larger
 269 than a few hundred meters in rocks and larger than a few meters in consolidated soil). The transition
 270 between porous and non-porous scaling law is considered linear (see Le Feuvre et al., 2011). The
 271 choice between the two different scaling laws proposed by Holsapple and Housen (2007) has
 272 important implications on the resulting age. In fact, the same measured CSFD will give a
 273 substantially older age if fitted assuming a cohesive soil/porous material rather than a non-
 274 porous/hard rock target. This considerable age difference results from the fact that porous target
 275 dissipates the impactor energy more efficiently than does the non-porous one. Therefore, for given
 276 impactor masses and velocities, craters formed on porous material will be smaller than those formed
 277 on hard rock (Holsapple and Housen, 2007; van der Bogert et al., 2017 and reference therein).
 278 In this work, we decided to consider the LWPF porous scaling law results, rather than the non-
 279 porous ones, for the reasons discussed below.

280 The thrust systems considered cross prevalently intercrater plains, densely cratered and then highly
 281 fractured. Moreover, the greater part of craters considered in the count has generally moderate
 282 dimensions, with diameters ranging between 1 km and 20 km. Such range of crater diameters is
 283 lower than that proposed by LeFeuvre and Wieckzoreck (2011) for non-porous regime (i.e.
 284 diameter >20 km). Indeed, according to Holsapple (1993), for complex craters, the relationship
 285 between the observed crater diameter (D) and the transient crater diameter (D_t) is:

286

$$\frac{D}{D_t} = 1.02 \left(\frac{D}{D_*} \right)^{0.079}$$

287

288

289 where D^* is the transition diameter between simple and complex crater, that on Mercury
290 corresponds to 10.3 km (Pike, 1988).

291 The ratio between the depth (H_t) and the diameter (D_t) of the transient crater is estimated to be
292 between 1/3 and 1/4 (Melosh and Ivanov, 1999). Then, for craters with an observed diameter of 20
293 km, the maximum excavation depth, H_t , ranges between 6.2 km and 4.6 km.

294 Schultz (1993) estimated a thickness of 4.5 km for the upper fractured bedrock layer on Mercury,
295 due to the cooling joints and fractures of basalts. However, it is likely that the subsequent impacts
296 caused a thickening of this fractured bedrock, especially in the old intercrater plains. Therefore, it is
297 probable that all the counted craters involved only the upper heavily fractured surface of the planet.

298 This evidence led us to consider the porous scaling law as the most suitable for our age estimation.

299 This is further confirmed by a comparison between the LWPF best fits performed with porous and
300 non-porous scaling law. Indeed, we observed that, for all the systems, the porous isochrons fit better
301 with our CSFDs rather than the non-porous ones, giving smaller errors on the age estimation.

302 Finally, if we consider the non-porous scaling law, for the Thakur and Victoria systems the
303 relationship between thrust's age and maximum age limit would not be respected.

304 The porous material scaling law was employed also to date the crater floors, and smooth plains
305 infilling the basin. Although in this latter case non-porous material seems to be the most appropriate
306 scaling law to use, also in this case basalt materials are highly fractured at the surface due to
307 pervasive jointing by cooling of the lavas (Schultz, 1993). Therefore, a cohesive soil/porous
308 material scaling law is more representative of these types of terrain considering the small dimension
309 of the counted craters (less than 10 km) (Giacomini et al., 2015).

310

311

312

313

314 3. Thrust systems description and their model age estimation

315

316

317 Based on the criteria described in Section 2, we detected five long thrust systems. We refer here to
318 each of them by the name of a prominent feature encompassed by the system, such a rupes or large
319 crater. The following names of the system are informal (i.e. not included in the USGS Gazetteer of
320 Planetary Nomenclature).

321 The ages obtained for each thrust system, considering the $S_{buffer}=2R+0.5W$ and the LWPF and
322 NPF age models, are listed in Table 1. For LWPF, both the porous material and the non-porous
323 material scaling law are reported in that table. However, in the following sections only porous
324 scaling law results are considered and discussed. The best fits of CSFDs with LWPF non-porous
325 scaling law are included in the supplementary material.

326 The ages obtained considering the $S_{buffer}=R+0.5W$ did not show significant difference with
327 respect to the first approach and they are reported in the supplementary material as well.

328 Since only the undeformed craters that overlap the thrust were counted, by applying the BCC
329 technique we estimated the age of the final stage of thrust activity. In addition to the BCC results,
330 also the maximum and minimum age limit, obtained by dating a faulted and an unfaulted crater
331 respectively, are reported. To gain maximum and minimum ages a traditional CSFD measurement
332 was used.

333

334 3.1 Thakur system

335

336 This system, located between 9.93°N and 23.78°S , 74.13°W and 60.10°W , is constituted by
337 eighteen structures for a total length of 1600 km. It cuts a crater of 104 km of diameter, called
338 Thakur. Hence, we refer here to this system as “Thakur thrust system” (Fig. 2).

339 The structures cut different terrains, from intercrater plains to smooth plains, these latter with
340 modest extension and emplaced within largest craters.

341 The tectonic structures are uniformly NNE-SSW oriented and their slope asymmetry suggests a NW
342 vergence. Locally, in particular in correspondence of four craters (i.e. Thakur crater, and three
343 unnamed craters, Fig.2), the thrusts show an opposite vergence. The southernmost lobate scarp
344 constituting the system is a basin-edge lobate scarp formed at the edge of a smooth plain infilling
345 the 340 km diameter Raphael basin.

346

347 3.1.1 Thakur system's age

348

349 A total amount of 30 craters overlapping Thakur system were counted (Fig.3a). By comparing the
350 CSFD with the LWPF the age obtained for the thrust is $3.7 (+0.03/-0.06)$ Ga (Fig.3d).

351 By considering the NPF we obtain $3.6 (+0.04/-0.06)$ Ga, which is concordant with the age gained
352 with LWPF (Fig.3e).

353 To obtain the maximum age limit for the system's activity we choose to date the floor of Thakur
354 crater, which is filled with a smooth plain deformed by structures (Fig.3b).

355 The age obtained with LWPF is $3.7 (+0.01/-0.02)$ Ga, suggesting a sin-deformational origin for the
356 crater (Fig. 3d). Following NPF, we obtained instead an age of 3.8 ± 0.02 Ga (Fig. 3e).

357 To obtain a minimum age for the system's activity we need to date an unfaulted crater. However,
358 the craters overlaying structures are not large enough to perform CSFD measurements, or their floor
359 is covered by clusters of secondary craters. Therefore, we chose to date the floor of a crater located
360 at about 50 km from the system but whose ejecta clearly mantle the north-central structures. The
361 crater, 50 km in diameter, shows a very sharp morphology, a very smooth floor and extended ejecta
362 (Fig.3c). As expected, the crater floor results very young: 84 ± 20 Ma according to LWPF (Fig. 3d).
363 By using NPF we obtained instead an older age of 260 ± 60 Ma (Fig.3e). The time span provided is
364 quite wide suggesting that the crater formed well after the end of thrust system activity.

365

366 3.2 Victoria system (extended)

367

368

369 This system is located between 65.00°N and 11.52°S and 35.92°W and 10.87°W . It represents the
370 longest system considered in this work covering a length of about 3500 km from the northern to the
371 southern end (Fig. 4). The northern part (encompassed between $58^{\circ}24'\text{N}$ and 22°N) is based on the
372 geological map of Galluzzi et al. (2016b) and has been already analyzed by Galluzzi et al. (2016a,
373 2019). In this work we considered also the southern extension of the system. The overall system is
374 constituted by forty-eight mapped thrusts, crossing in large part heavily cratered intercrater plains.
375 The longest thrust within the system is the 550 km-long Victoria Rupes, from which we took the
376 name for the system as a whole. Other long lobate scarps are included in the system, as Antoniadi
377 Dorsum, Endeavour and Santa Maria rupes (Fig. 4b). The structures included in the system show a

378 prevalent N–S orientation in the northern and central sector, changing slightly to NNW–SSE toward
379 south to return N–S at the southern tip. Some of the thrusts follow the crater rims, suggesting that
380 they developed along previous impact discontinuities. The system verges mainly toward east,
381 although several changes in vergence are locally observable. In fact, in correspondence of the
382 central and southern part of the system some back thrusts are observed in association with the main
383 thrust. Moreover, like in the case of Thakur system, the structures show opposite vergence in
384 correspondence with five craters (Fig.4).

385

386 3.2.1 Victoria system's age

387

388 In order to date the Victoria system 114 craters were counted (Fig. 5a). We then obtained an age of
389 about 3.7 (+0.02/–0.02) Ga for LWPF. With NPF we obtained an age similar to the first case,
390 attested at 3.8 ± 0.02 Ga (Fig. 5d,e).

391 To obtain a maximum age limit of the system's activity we chose a faulted central peak crater
392 named Donne, of about 85 km in diameter (Fig. 5b). We chose it among the other faulted craters
393 since its floor does not appear to be affected by ejecta of surrounding craters, and then the effect of
394 secondaries on the age estimation should be minimized. The crater count of the floor gave a
395 maximum age limit of 3.8 (+0.01/–0.02) Ga with LWPF, similar to the 3.9 ± 0.02 Ga obtained with
396 NPF (Fig.5d and e respectively).

397 The superposed craters that are suitable to obtain the minimum age limit for Victoria system (i.e.
398 with a crater floor large enough for a good statistic and not affected by secondaries) were lacking.
399 For this reason, we choose a central peak crater that does not directly overlap the structures but lays
400 over a 25km-diameter crater whose rim covers a structure located in the central part of the system.
401 The chosen crater has a diameter of 67 km and shows a well preserved rim and clearly visible
402 proximal ejecta (Fig.5c). The crater counting of the crater's floor gave an age of 2.4 ± 0.4 Ga with
403 LWPF (Fig. 5d). With NPF the age was instead $3.5 (+0.05/-0.08)$ Ga (Fig.5e).

404

405 3.3 Villa Lobos system

406

407

408 The system is located between 23.63°N and 1.95°N and 3.45°E and 15.28°E for a maximum N–S
409 extent of about 900 km (Fig. 6). It encompasses twenty-five thrusts, one of them cutting the Villa
410 Lobos crater. Therefore, we refer here to the system as Villa Lobos system.

411 It shows a general N–S orientation with a westward vergence. Such a vergence is kinematically in
412 agreement with the slight change in trend of the southern structures (NW–SE), likely representing
413 lateral ramps of the system, linked with the frontal thrust. In correspondence with three unnamed
414 craters (Fig. 6) thrusts show an opposite vergence. In two of these craters thrusts are observed to
415 follow crater margins, suggesting that they follow pre-existing zones of weakness. Back-thrusts are
416 detected in association to some of the main faults, frequently in the eastern part of the system. The
417 thrust system cuts a variety of terrains, from intercrater plains to large craters filled with smooth
418 plains. The eastern part of the system, in particular, cuts an extended less cratered region, likely the
419 result of a resurfacing process.

420

421 3.3.1 Villa Lobos system's age

422

423 For Villa Lobos system 18 craters were considered for the BCC (Fig.7a). The end of activity of the
424 system has been dated at about 3.6 (+0.09/−0.8) Ga with LWPF, an age similar to that obtained with
425 NPF, attested at about 3.6 (+0.06/−0.01) Ga (Fig.7d-e).

426 For the maximum age limit we dated the floor of a large faulted crater with a diameter of about 120
427 km, located in the central sector of the system. It shows a moderately degraded crater rim and
428 proximal ejecta (Fig. 7b). We obtained an age of 3.7 (+0.02/−0.03) Ga with LWPF and 3.9 (+0.04/−
429 0.05) Ga with NPF (Fig.7d and e, respectively).

430 Concerning the minimum age limit, the superposed craters larger enough to be suitable for a
431 traditional CSFD measurement were very few. One of the larger superposed crater located in the
432 northern sector of the system has the floor heavily affected by chains or clusters of craters, likely
433 due to the ejecta of subsequent craters. The presence of such secondary craters could invalidate the
434 count. For this reason we decided to consider a crater named Kyosai (Fig.7c), located immediately
435 on the west side of this larger crater and whose ejecta superpose its rim. However, the floor of
436 Kyosai shows extended areas of hollows. Therefore, the age of this surface can be compromised.
437 For this reason the ejecta of the crater were considered for CSFD measurements, obtaining and
438 absolute model age of 1.3 ± 0.4 Ga, following LWPF (Fig. 7d). Following instead NPF, the age gap
439 between the final stage of the system activity and the superposed crater is shorter, since the model
440 assigns an age of 3.4 (+0.1/−0.5) Ga (Fig.7e).

441

442

443 3.4 Al-Hamadhani system

444

445 This thrust system extends between 42.63°N and 12.02°N and 99.44°W and 83.22°W and includes
446 twenty-four structures, for a total length of about 1500 km. One of its lobate scarps cuts a crater
447 named Al-Hamadhani, from which the system has been named (Fig.8).

448 The lobate scarps crosscut intercrater plains but also several large basins whose floor is covered by
449 smooth plains.

450 In the south-western part, the lobate scarps also cut an extended area characterized by a lower crater
451 density with respect to the surrounding area and which is probably constituted by volcanic deposits
452 as well.

453 The system shows a general NE–SW orientation and a vergence toward NW. Also in this system,
454 structures with opposite vergence (i.e. SE) have been observed on five unnamed craters. Locally,
455 the main thrust is associated with back-thrusts, in particular approaching some of the crater rims.

456

457 3.4.1 Al-Hamadhani system's age

458

459 To determine an absolute model age for the Al-Hamadhani system 43 craters were included in the
460 BCC measurement (Fig. 9a). The BCC method established the final stage of the activity at about 3.7
461 (+0.02/−0.03) Ga for LWPF (Fig. 9d). An age of 3.8 ± 0.03 Ga was obtained instead with NPF (Fig.
462 9e).

463 The maximum age limit for system's activity was derived by counting the floor of a large faulted
464 crater, 116 km in diameter, showing signs of erosion but with a still preserved crater rim and
465 remnants of the ejecta blanket (Fig.9b). We obtained an age of about 3.8 (+0.01/−0.02) Ga
466 following LWPF (Fig. 9d); NPF gave an age of 3.9 (+0.02/−0.03) Ga (Fig.9e).

467 To obtain the minimum age limit, we dated the ejecta of a crater with a diameter of 30 km that
468 overlays the central segment of the system. It shows a well preserved rim, a central peak and
469 proximal ejecta (Fig.9c). The count gave an age of 100 ± 40 Ma for LWPF (Fig. 9d), with NPF we
470 obtained instead an age of 300 ± 100 Ma (Fig.9e). Also in this case the time span between the age of
471 the final stage of thrust's activity and the minimum age limit is considerably wide.

472

473 3.5 Enterprise system

474

475 This thrusts system represents the surface expression of a large-scale thrust fault (Fig. 10).
476 Topographic and kinematic analyses attest that this system includes Enterprise Rupes, one of the
477 longest thrust known on Mercury (Watters et al, 2009a; Ferrari et al., 2015; Massironi et al., 2015),
478 from which we took our name for the system. It is located between 25.47°S and 38.68°S and 64.89°
479 E and 84.23°E , for a total length of 820 km. This system transects the Rembrandt basin and
480 includes two segments, one inside and one outside the crater, which show different characteristics.
481 Indeed, on the western branch, outside the basin, the system has a WSW–ENE orientation whereas
482 on the eastern branch, in the basin's floor, the orientation changes in SW–NE (Ferrari et al., 2015;
483 Galluzzi et al., 2015). Several strike-slip kinematic indicators have been observed along the thrusts
484 suggesting a dextral transpression in the western branch and a sinistral transpression in the eastern
485 one. This, coupled with the arcuate shape in plan view and the asymmetric relief of the thrusts,
486 indicates a SE vergence for the Enterprise system (Galluzzi et al., 2015; Massironi et al., 2015).
487 The system crosses different types of material: from heavily cratered terrains, outside the
488 Rembrandt basin, to smooth plains within the Rembrandt basin.

489

490 3.5.1 Enterprise system's age

491

492 The craters counted to date the Enterprise system are 22 (Fig.11a). The age obtained with LWPF for
493 the Enterprise system is $3.7 (+0.03/-0.04)$ Ga (Fig. 11d). By following NPF we obtain an age of 3.8
494 $(+0.05/-0.08)$ Ga (Fig.11e).

495 The maximum age limit can be provided by the Rembrandt basin. As highlighted by Ferrari et al.
496 (2015), Rembrandt inner plains are constituted by different subunits. Therefore, a CSFD of the
497 Rembrandt floor would not be representative of the younger resurfacing event alone, but of more
498 than one event. For this reason we chose to date the Rembrandt basin itself. Ferrari et al. (2015)
499 already performed the crater counting for the Basin related Material (*BM*) that includes the basin's
500 proximal ejecta and hummocky unit, interpreted to be a mixture of impact melt and ejecta (Fig.11b).
501 The age obtained for *BM* was 3.85 ± 0.1 Ga, following NPF (Fig. 11f). In this work we considered
502 the same crater count, obtaining a comparable age of 3.8 ± 0.007 Ga for the LWPF (Fig. 11d).
503 For the minimum age the only superposing crater whose floor is big enough to be dated is located in
504 the northern sector of Enterprise Rupes. It has a diameter of about 23 km and shows a sharp
505 morphology (Fig. 11c). The result of the crater count gave an age of 950 ± 200 Ma with LWPF (Fig.
506 11d) and 2.0 ± 0.4 Ga (Fig. 11f) following NPF (Fig. 11e).

507

508

509 4. Discussion

510

511 The results obtained with the BCC technique revealed that the systems taken into account in this
512 work ended their activity into a time range of 3.6–3.7 Ga, following LWPF, and 3.6–3.8 Ga,
513 considering NPF. A further discussion about the age differences observed between LWPF and NPF
514 is included in the supplementary material.

515 The results obtained for the thrust systems are in agreement with the age estimated previously for
516 other Mercurian systems, as the Blossom thrust system, whose activity was estimated to end at
517 about 3.5–3.7 Ga, according to the Model Production Function (cohesive soil) proposed by Marchi
518 et al. (2009) and NPF, respectively (Giacomini et al., 2015). Addition of the Blossom system to the
519 five systems reported here allows a more complete global assessment of major tectonic systems that
520 occurred on Mercury.

521 These results are also in agreement with the classical stratigraphic analysis between lobate scarps
522 and craters performed by Banks et al. (2015). They estimated that the fault activity should have
523 occurred by a time near to the Late Heavy Bombardment (LHB) (i.e. an increasing of impacts
524 registered on lunar surface probably due to an injection in the inner system of main belt and/or
525 Kuiper belt objects, occurred at about 4.0 Ga according to Marchi et al., 2013). In fact, they
526 observed that some lobate scarps appear superposed by undeformed Calorian craters (Calorian
527 system covers a time span between 3.9 Ga and 3.5–3.0 Ga). Banks et al. (2015) also observed that
528 some lobate scarps continue their activity until recent age, since some small (< 3 km) fresh craters
529 appear modified or cut by scarps. This is in agreement with the discovery of some thrusts
530 interpreted to be Kuiperian in age on the basis of crater degradation morphologies (Watters et al.,
531 2015). Such a long-lived tectonic activity is not in contrast with our results since the ages we
532 obtained using the BCC method for each system represent the final major activity recorded for the
533 system as a whole, but more recent movements could have been occurred in some single thrusts.
534 Anyway, the results suggest that the tectonic activity giving rise to lobate scarps took place very
535 early in Mercury's history, well before than previously hypothesized by thermophysical models
536 (Tosi et al., 2013). According to these models, the tectonism of Mercury is intimately related with
537 the beginning of the contraction of the planet due to the core's cooling process. This contraction has
538 been estimated to start at about 3 Ga, well after the LHB (Grott et al, 2011; Tosi et al., 2013). Our
539 results, however, would suggest that the activity responsible for the lobate scarps growth began
540 earlier in Mercury's history, at least before 3.6 Ga.

541 This means that the actual thermal model for the planet should be modified changing some
542 parameters, like mantle temperature and viscosity or thickness of the regolith layer, in order to
543 allow an earlier contraction.

544 On the other hand, the results obtained in this work could suggest that these major thrust systems
545 formed in response to other processes, like tidal despinning (e.g. Klimczak et al., 2015), but also
546 mantle downwelling (Massironi et al., 2015; Watters et al., 2015), which then could have played a
547 role on the structures formation and then on Mercury's evolution.

548 Such hypothesis seems to be confirmed also by the age estimated for the extended smooth plains,
549 which assesses the end of the widespread effusive volcanism at about 3.5 Ga (Byrne et al., 2016).
550 Indeed, the end of the extensive volcanism corresponds with the progressive contraction of the crust
551 and the consequent closure of the conduits that allow the rising of magma toward the surface.

552 Therefore, large volume effusive volcanism is not expected to occur after the beginning of the
553 global contraction (Wilson and Head, 2008; Byrne et al., 2016). However, this is not in agreement
554 with the age obtained in this work for the end of thrust system's activity (3.6–3.7 Ga). Then, if the
555 beginning of the contraction occurred after 3.5 Ga, as suggested by the thermophysical models and

556 Byrne et al.'s results, it is likely that the thrust systems considered in this work formed in response
557 to other processes.

558 Moreover, the thrust systems are mainly located in the lower latitudes and show a prevalent N-S
559 orientation (Fig. 12), in accordance with the scenario predicted by Klimczak et al. (2015) that, on
560 the basis of stress' magnitude and latitudinal variation, theorized a higher density and larger
561 dimension of structures at the equatorial zone. Furthermore, the systems show a concentration in
562 longitudinal bands, in agreement with Watters et al. (2015) that observed a non-uniform spatial and
563 aerial distribution of the largest tectonic structures. It seems also that the systems show a regular
564 longitudinal framework. Such a pattern could represent evidence that mantle convection, with
565 regularly-spaced linear convection planforms, could have been involved in the first stages of
566 Mercury's evolution, as suggested by King (2008). Alternatively, it can be expression of variations
567 on the lithospheric strength (Watters et al., 2015).

568 The detection of strike-slip kinematic indicators, that cannot be explain with the solely contraction,
569 seems to confirm the hypothesis that other mechanisms should be invoked to explain the Mercury's
570 tectonic framework (Massironi et al., 2015).

571

572

573 5. Conclusions

574

575 Five long thrust systems have been identified and dated through the buffered crater counting (BCC)
576 technique in order to temporally constrain their activity. Two different chronology models were
577 adopted: LeFeuvre and Wieczorek Production Function and the Neukum Production Function. For
578 the former an age ranging between 3.6 Ga and 3.7 Ga (porous scaling law) was obtained, whereas
579 for the latter one a slightly wider range of 3.6–3.8 Ga has been estimated. To date the systems, only
580 unfaulted craters were counted, therefore the age obtained indicate the final stage of the activity
581 registered along the thrust systems, when the associated stress was insufficient to cause the
582 deformation of craters located along their strike. The resulted thrusts systems' ages are coherent
583 with the classical stratigraphic approach, as they are set between the faulted and unfaulted crater's
584 age. That comparability would support the effectiveness of the BCC technique as a method to date
585 thrust systems. Such results have important implications regarding the thermal evolution of
586 Mercury since they provide new clues on what occurred during the first stage of the planet's
587 history. Indeed, their early formation (well before than predicted by the thermophysical models), the
588 chronological relationships with widespread effusive volcanism, their non-random orientation and
589 spatial distribution, suggest that they can be formed with the contribution of other processes beside
590 global contraction. This leads us to hypothesize that mantle downwelling or tidal despinning, could
591 have contribute to the planet's evolution.

592 A significant finding is that all the thrust systems ended their activity at about the same time, rather
593 early on the planet evolution. This would suggest that the higher strains exceeding the frictional
594 resistance of the lithosphere, causing the surface breaking at large scale (and then the formation of
595 systems of thrusts) occurred prevalently early in the planet history. This seems in agreement with
596 hypothesis that higher strain rate occurred on Mercury prior to 3.9–3.5 Ga, and decreased over the
597 time (Phillips and Solomon, 1997; Klimczak , 2015).

598

599 *Acknowledgments*

600

601 *We thank A. Nahm, J. Clark and an anonymous reviewer who provided detailed and helpful*
 602 *suggestions*
 603 *that improved the quality of the manuscript. Part of this work was funding from the Italian Space*
 604 *Agency (ASI) under ASI-INAF agreement 2017-47-H.O.*

605
 606

607 *References*

608

609 Banks M.E., Klimczak C., Xiao Z., Watters T.R., Strom R.G., Braden S.E., Chapman C.R., Solomon S.C.,
 610 Byrne P.K., 2014. Duration of activity on lobate-scarp thrust faults on Mercury. *Lunar Planet. Sci.*45,
 611 abstract 2722.

612 Beuthe, M., 2010. East–west faults due to planetary contraction. *Icarus*, 209, 795–817

613 Bouley, S., Craddock, R.A., Mangold, N., & Ansan, V. 2010. Characterization of fluvial activity in Parana
 614 Valles using different age-dating techniques. *Icarus*, 207(2), 686-698.

615 Burns J.A., 1976. Consequences of the tidal slowing of Mercury. *Icarus*, 28, 453–458.

616 Byrne, P.K., Klimczak, C., Şengör, A.M.C., Solomon, S.C., Watters, T.R., & Hauck, S.A. 2014. Mercury’s
 617 global contraction much greater than earlier estimates. *Nature Geoscience*, 7, 301–307.

618 Byrne P. K., Ostrach L. R., Fassett C. I., Chapman C. R., Denevi B. W., Evans A. J., Klimczak C., Banks M.
 619 E., Head J. W., Solomon S. C., 2016. Widespread effusive volcanism on Mercury likely ended by about
 620 3.5 Ga. *Geophys. Res. Letters*, 43 (14), 7408-7416.

621 Clark J.D., Hurtado Jr. J.M., Hiesinger H., Bernhardt H., van der Bogert C.H., 2017. Investigation of lobate
 622 scarps: Implications for the tectonic and thermal evolution of the Moon. *Icarus*, 298, 78-88.

623 Denevi B. W., Ernst C.M., Meyer H.M., Robinson M.S., Murchie S.L., Whitten J.L., Head J.W., Watters
 624 T.R., Solomon S.C., Ostrach L.R., Chapman C.R., Byrne P.K., Klimczak C., Peplowski P.N., 2013. The
 625 distribution and origin of smooth plains on Mercury, *J. Geophys. Res. Planets*, 118, 891–907.

626 Dombard, A. J. & Hauck, S. A. 2008. Despinning plus global contraction and the orientation of lobate scarps
 627 on Mercury. *Icarus*, 198, 274–276.

628 Dzurisin, D., 1978. The tectonic and volcanic history of Mercury as inferred from studies of scarps, ridges,
 629 troughs, and other lineaments. *J. Geophys. Res.*, 83, 4883-4906.

630

631 Fassett, Caleb I., Head, & James W. 2008. Valley network-fed, open-basin lakes on Mars: Distribution and
 632 implications for Noachian surface and subsurface hydrology. *Icarus*, **198**, 37-56.

633

634 Fassett, C.I., Head, J.W., Baker, D.M.H., Zuber, M.T., Smith, D.E., Neumann, G.A.; Solomon, S.C.,
 635 Klimczak, C., Strom, R.G., Chapman, C.R., Prockter, L.M., Phillips, R.J., Oberst, J., & Preusker, F. 2012.
 636 Large impact basins on Mercury: Global distribution, characteristics, and modification history from
 637 MESSENGER orbital data. *Journal of Geophysical Research*, 117, E00L08, doi:10.1029/2012JE004154.

638

639 Fegan E. R., Rothery D. A., Marchi S., Massironi M., Conway S. J., Anand, M., 2017. Late movement of
 640 basin-edge lobate scarps on Mercury. *Icarus*, 288, 226-234.

641

642 Ferrari S., Massironi M., Marchi S., Byrne P.K., Klimczak C., Martellato E., Cremonese G., 2015. Age
 643 relations of Rembrandt basin and Enterprise Rupes, Mercury. In: Platz, T., Massironi, M., Byrne, P.K.,
 644 Hiesinger, H. (Eds.), *Volcanism and Tectonism across the Inner Solar System*. In: *Geol. Soc. London*
 645 *Spec. Pub.*, 401, 159–172.

- 646
647 Giacomini L., Massironi M., Marchi S., Fassett C. I., Di Achille G., Cremonese G., 2015. Age dating of an
648 extensive thrust system on Mercury: implications for the planet's thermal evolution. In: Platz, T.,
649 Massironi, M., Byrne, P.K., Hiesinger, H. (Eds.), *Volcanism and Tectonism across the Inner Solar*
650 *System*. In: *Geol. Soc. London Spec. Pub.*, 401, 291-311.
651
- 652 Galluzzi V., Di Achille G., Ferranti L., Popa C., Palumbo P., 2015. Faulted craters as indicators for thrust
653 motions on Mercury. In: Platz, T., Massironi, M., Byrne, P.K., Hiesinger, H. (Eds.), *Volcanism and*
654 *Tectonism across the Inner Solar System*. In: *Geol. Soc. London Spec. Pub.*, 401, 313–325. Galluzzi V.,
655 Ferranti L., Guzzetta L., Giacomini L., Massironi M., Palumbo P., 2016a. Investigating the Architecture
656 and Evolution of the Victoria Rupes — Antoniadi Dorsum Array, Mercury. 47th Lunar and Planetary
657 Science Conference. LPI Contribution No. 1903, p.2164.
- 658 Galluzzi, V., L. Guzzetta, L. Ferranti, G. Di Achille, Rothery, D. A., & P. Palumbo, 2016b. Geology of the
659 Victoria quadrangle (H02), Mercury. *J. Maps*, 12, 227–238.
- 660 Galluzzi V., Ferranti L., Massironi M., Giacomini L., Guzzetta L., Palumbo P., 2019. Structural analysis of
661 the Victoria quadrangle fault systems on Mercury: timing, geometries, kinematics and relationship with
662 the high-Mg region. *Journal of Geophysical Research: Planets*, under review.
- 663 Gault, D. E.; Guest, J. E.; Murray, J. B.; Dzurisin, D.; Malin, M. C., 1975. Some comparisons of impact
664 craters on Mercury and the Moon. *J. Geophys. Res.*, 80, 1975, 2444-2460.
- 665 Grott, M., Breuer, D., & Laneuville, M. 2011. Thermo-chemical evolution and global contraction of
666 mercury. *Earth and Planetary Science Letters*, 307(1), 135-146.
- 667 Hartmann, W.K. 1977. Relative crater production rates on planets. *Icarus*, 31, 260-276.
- 668 Hauck, S. A., Dombard, A. J., Phillips, R. J., & Solomon, S. C. 2004. Internal and tectonic evolution of
669 Mercury. *Earth and Planetary Science Letters*, 222, 713–728.
- 670 Hoke, M.R.T., & Hynek, B.M. 2009. Roaming zones of precipitation on ancient Mars as recorded in valley
671 networks. *Journal of Geophysical Research*, 114. doi:10.1029/2008JE003247.
- 672 Holsapple, K. A., 1993. The scaling of impact processes in planetary sciences. *Annual review of earth and*
673 *planetary sciences*, 21 (A94-10876 01-91), 333-373.
- 674 Holsapple, K.A., & Housen, K.R. 2007. A crater and its ejecta: an interpretation of deep impact. *Icarus*, 187,
675 345–356.
- 676 King, S. D. 2008, Pattern of lobate scarps on Mercury's surface reproduced by a model of mantle
677 convection. *Nature Geoscience*, 1, 229-232.
- 678 Klimczak C., Byrne P. K., Solomon S. C., 2015. A rock-mechanical assessment of Mercury's global tectonic
679 fabric, *Earth Planet. Sci. Lett.*, 416, 82–90.
- 680 Klimczak C., 2015. Limits on the brittle strength of planetary lithospheres undergoing global contraction. *J.*
681 *Geophys. Res.: Planets*, 120 (12), 2135-2151.
- 682 Kneissl T., van Gasselt S., Neukum G., 2011. Map-projection-independent crater size-frequency
683 determination in GIS environments — New software tool for ArcGIS. *Planetary and Space Science*, 59,
684 1243-1254, DOI: 10.1016/j.pss.2010.03.015, 2011.

- 685 Kneissl T., Michael G. G., Platz T., Walter S. H. G., 2015. Age determination of linear surface features using
686 the Buffered Crater Counting approach - Case studies of the Sirenum and Fortuna Fossae graben systems
687 on Mars. *Icarus*, 250, 384-394.
- 688 Le Feuvre M., Wieczorek M. A., 2011. Nonuniform cratering of the Moon and a revised crater chronology of
689 the inner Solar System. *Icarus*, 214 (1), 1-20.
- 690 Marchi S., Mottola S., Cremonese G., Massironi M., Martellato E., 2009. A New Chronology for the Moon
691 and Mercury. *The Astronomical Journal*, 137, 4936-4948.
- 692 Marchi S., C. R. Chapman, C. I. Fassett, J. W. Head, W. F. Bottke, and R. G. Strom, 2013. Global
693 resurfacing of Mercury 4.0–4.1 billion years ago by heavy bombardment and volcanism. *Nature*, 499, 59–
694 61, doi:10.1038/nature12280.
- 695 Massironi M., Di Achille G., Rothery D., Galluzzi V., Giacomini L., Ferrari S., Zusi M., Cremonese G.,
696 Palumbo P., 2015. Lateral ramps and strike-slip kinematics on Mercury. In: Platz, T., Massironi, M.,
697 Byrne, P.K., Hiesinger, H. (Eds.), *Volcanism and Tectonism across the Inner Solar System*. In: Geol. Soc.
698 London Spec. Pub., 401, 269–290.
- 699 Matsuyama, I., Nimmo, F., 2009. Gravity and tectonic patterns of Mercury: effect of tidal deformation,
700 spin-orbit resonance, nonzero eccentricity, despinning, and reorientation. *J. Geophys. Res.* 114, E01010.
701 <http://dx.doi.org/10.1029/2008JE003252>.
- 702 Melosh, H. J., & Dzurisin D. 1978, Mercurian global tectonics - A consequence of tidal despinning. *Icarus*,
703 35, 227-236.
- 704 Melosh H.J., 1977. Global tectonics of a despun planet. *Icarus*, 31, 221–243.
- 705 Melosh, H. J., & McKinnon, W. B. 1988. The tectonics of Mercury. In: Vilas, F., Chapman, C.R., Matthews,
706 M.S. (Eds.). *Mercury*. The University of Arizona Press.
- 707 Melosh, H.J. 1989. *Impact Cratering: A Geologic Process*. Oxford University Press, New York, 245.
- 708 Melosh H. J., Ivanov B. A., 1999. Impact Crater Collapse. *Annual Review Of Earth And Planetary Sciences*,
709 27, 385-415.
- 710 Michael, G. G., & Neukum, G. 2010. Planetary surface dating from crater size-frequency distribution
711 measurements: Partial resurfacing events and statistical age uncertainty. *Earth and Planetary Science*
712 *Letters*, 294(3-4), 223-229.
- 713 Neukum, G. 1983. *Meteoriten bombardement und Datierung planetarer Ober flachen*. Habilitation,
714 University of Munich, February.
- 715 Neukum, G., & Ivanov, B. 1994. Crater Size Distributions and Impact Probabilities on Earth from Lunar,
716 Terrestrial-planet, and Asteroid Cratering Data. In: Tom Gehrels, M. S. Matthews. and A. Schumann,
717 *Hazards due to comets and asteroids*, Space Science Series, Tucson, AZ. Edited by Published by
718 University of Arizona Press, 1994, 359.
- 719 Neukum, G., Ivanov, B. A., Hartmann, W. K. 2001a. Cratering Records in the Inner Solar System in
720 Relation to the Lunar Reference System. *Space and Science Reviews*, 96, 55.
- 721 Neukum, G., Oberst, J., Hoffmann, H., Wagner, R., & Ivanov, B. A 2001b. Geologic evolution and cratering
722 history of Mercury. *Planetary and Space Science*, 49(14-15), 1507-1521.

- 723 Pechmann, J. B., & Melosh, H. J. 1979. Global fracture patterns of a despin planet application to Mercury.
724 Icarus, 38, 243–250.
- 725 Phillips R. J., Solomon S. C., 1997. Compressional strain history of Mercury. 28th Annual Lunar and
726 Planetary Science Conference, LPI Contribution n. 1572, 1107-1108.
- 727 Platz, T., Michael, G., Tanaka, K. L., Skinner, J.A. & Fortezzo, C. M. 2013. Crater-based dating of
728 geological units on Mars: methods and application for the new global geological map. Icarus, 225, 806–
729 827.
- 730 Schubert, G., Ross, M. N., Stevenson, D. J., & Spohn, T. 1988. Mercury's thermal history and the generation
731 of its magnetic field. In: Vilas, F., Chapman, C.R., Matthews, M.S. (Eds.). Mercury. The University of
732 Arizona Press.
- 733 Schultz, R.A. 1993. Brittle Strength of Basaltic Rock Masses with Applications to Venus. Journal of
734 Geophysical Research, 98(E6), 10883-10895.
- 735 Senthil Kumar P., Sruthi U., Lakshmi K.J.P., Menon R., Amitabh Krishna B.G., Kring D.A., Head J.W.,
736 Goswami J.N., Kumar A.S.K., 2016. Recent shallow moonquakes and impact-triggered boulder falls on
737 the Moon: New insights from the Schrödinger basin. J. Geophys. Res., 121, 147-197.
- 738 Solomon, S. C. 1976. Some aspects of core formation in Mercury. Icarus, 28, 509–521.
- 739 Solomon, S. C. 1977. The relationship between crustal tectonics and internal evolution in the Moon and
740 Mercury. Physics of the Earth and Planetary Interiors, 15, 135–145.
- 741 Strom, R. G., Trask, N. J., and Guest, J. E., 1975. Tectonism and volcanism on Mercury. J. of Geophys. Res.,
742 80, 2478–2507.
- 743 Strom, R.G. & Neukum, G. 1988. The cratering record on Mercury and the origin of impacting objects, In:
744 Vilas, F., Chapman, C.R., Matthews, M.S. (Eds.), Mercury. The University of Arizona Press, 336-373.
- 745 Strom R.G., Banks M.E., Chapman C.R., Fassett C.I., Forde J.A., Head J.W., Merline W.J., Prockter L.M.,
746 Solomon S.C., 2018. Mercury crater statistics from MESSENGER flybys: Implications for stratigraphy
747 and resurfacing history. Planetary and Space Science, 59(15), 1960-1967.
- 748 Tanaka, K.L. 1982. A new time-saving crater-count technique with application to narrow features. NASA
749 Technical Memorandum, TM-85127, 123–125.
- 750 Tosi N., Grott M., Plesa A.-C., Breuer D., 2013. Thermochemical evolution of Mercury's interior. J.
751 Geophys. Res.: Planets, 118 (12), 2474-2487.
- 752 van der Bogert C. H., Hiesinger H., Dundas C. M., Krüger T., McEwen A. S., Zanetti M., Robinson M. S.,
753 2017. Origin of discrepancies between crater size-frequency distributions of coeval lunar geologic units
754 via target property contrasts. Icarus, 298, 49-63.
- 755 van der Bogert C.H.; Clark J.D.; Hiesinger H., Banks M.E., Watters T.R., Robinson M.S., 2018. How old are
756 lunar lobate scarps? 1. Seismic resetting of crater size-frequency distributions. Icarus, 306, 225-242.
- 757 Watters, T.R., Robinson, M.S., & Cook, A.C. 1998. Topography of lobate scarps on Mercury: New
758 constraints on the planet's contraction. Geology, 26, 991–994.

- 759 Watters T.R., Solomon S.C., Robinson M.S., Head J.W., André S.L., Hauck II S.A., Murchie S.L., 2009a.
 760 The tectonics of Mercury: the view after MESSENGER's first flyby. *Earth Planet. Sci. Lett.* 285, 283–
 761 296.
- 762 Watters T.R., Murchie S.L., Robinson M.S., Solomon S.C., Denevi B.W., André S.L., Head J.W., 2009b.
 763 Emplacement and tectonic deformation of smooth plains in the Caloris basin Mercury. *Earth and*
 764 *Planetary Science Letters*, 285(3-4), 309-319.
- 765 Watters, T.R., & F. Nimmo 2010. Tectonism on Mercury. In: R.A. Schultz and T.R. Watters, eds.,
 766 *Planetary Tectonics*, Cambridge Univ Press, 15- 80.
- 767 Watters T. R., Selvans M. M., Banks M. E., Hauck S. A., Becker K. J., Robinson M. S., 2015. Distribution of
 768 large-scale contractional tectonic landforms on Mercury: Implications for the origin of global stresses.
 769 *Geophys. Res. Letters*, 42, 10, 3755-3763.
- 770 Wichman, R.W., & Schultz, P.H. 1989. Sequence and mechanisms of deformation around the Hellas and
 771 Isidis impact basins on Mars. *Journal of Geophysical Research*, 94, 17333–17357.
- 772 Wilson L., Head J.W., 2008. Volcanism on Mercury: A new model for the history of magma ascent and
 773 eruption. *Geophysical Research Letters*, 35(23), CiteID L23205.
- 774 Xiao Z., 2018. On the importance of self-secondaries. *Geoscience Letters*, 5:17; doi: 10.1186/s40562-018-
 775 0116-9.
- 776 Yue Z., Michael G.G., Di K., Liu J., 2017. Global survey of lunar wrinkle ridge formation times. *Earth and*
 777 *Planet. Sci. Letters*, 477, 14-20.

778
 779
 780
 781
 782
 783
 784
 785
 786

Figure captions

- 787 Fig.1 Global view of the five thrust systems analyzed and dated in this work. The background is the MDIS
 788 global mosaic (spatial resolution 250 m/pixel) in equirectangular projection.
- 789 Fig.2 Thakur thrust system, named after the Thakur crater, which is cut by one of the structures included in
 790 the system (a). (b) Thakur system's structures (in red; triangles indicate the dip direction of the thrust), show
 791 a NW vergence. In correspondence of four craters (indicated by white arrows) the structures verge in the
 792 opposite direction (see text for more details). On the background is a MDIS BDR mosaic (166 m/pixel) in
 793 equirectangular projection.
- 794 Fig.3 Dating of Thakur thrust system. (a) Buffer areas (in green) created around lineaments (in red). Blue
 795 circles indicate the crater overlapping the structures and considered in the count to compile the final crater
 796 SFD and date the system. A faulted and an unfaulted crater were also chosen to estimate a maximum and a
 797 minimum age limit for the system and are indicated by a pink and a white arrow, respectively. (b) Enlarged
 798 view of Thakur crater. In blue are outlined the area chosen for the counting and in red are the counted
 799 craters. (c) Enlarged view of the chosen unfaulted crater (unnamed); the count was performed on a NAC
 800 image (EN1053868463M; 87 m/pixel). Symbology as in (b). The crater SFDs of the system (black squares),

801 of Thakur crater (red filled circles), and the unfaulted crater (green filled stars) were plotted and compared
802 with LWPF porous scaling law (d), and NPF (e) to obtain the absolute model age for the system.

803 Fig.4 (a) Victoria thrust system, named after Victoria rupes, the longest scarp encompassed in the system.
804 (b) Structures composing the system are outlined in red (triangles indicate the dip direction of the thrust).
805 The system shows an eastward vergence. In correspondence of five craters (indicated by white arrows), the
806 structures show an opposite vergence (see text for more details). On the background is a MDIS BDR mosaic
807 (166 m/pixel) in equirectangular projection.

808 Fig.5 Dating of Victoria thrust system. (a) Buffer areas (in green) created around lineaments (outlined in
809 red). Craters overlapping the structures and considered for the counting are outlined in blue. A pink and a
810 white arrow respectively indicate a faulted and an unfaulted crater chosen to estimate a maximum and a
811 minimum age limit for the system. (b) Enlarged view of the faulted crater (unnamed). In blue are outlined the
812 area chosen for the counting and in red are the counted craters. Count was performed on a NAC image
813 (EN1022397268M; 58 m/pixel). (c) Enlarged view of the chosen unfaulted crater (unnamed). Symbology as
814 in (b). Count was made on EN1067811079M NAC image (91 m/pixel). The crater SFDs of the system (black
815 squares), of the faulted crater (red filled circles), and unfaulted crater (green filled stars) were plotted and
816 compared with LWPF porous scaling law (d), and NPF (e) to obtain the absolute model age for the system.
817 NPF chart show a depletion of larger craters. This is possibly due to an underestimation of craters larger than
818 20 km superposed to the thrust system, although such depletion seems to not be observed on LWPF chart.

819 Fig.6 Villa Lobos thrust system, named after Villa Lobos crater (a). (b) Structures encompassed in the
820 system, outlined in red (triangles indicate the dip direction of the thrust), show a prevalent eastward
821 vergence. In association with three craters (indicated by white arrows), the structures show an opposite
822 vergence (see text for more details). On the background is a MDIS BDR mosaic (166 m/pixel) in
823 equirectangular projection.

824 Fig.7 Dating Villa Lobos thrust system. (a) Buffer areas (in green) created around lineaments (outlined in
825 red). Craters overlapping the structures and considered for the counting are outlined in blue. A pink arrow
826 indicates the faulted crater chosen for the maximum system's age limit; white arrow indicates Kyosai crater,
827 chosen to estimate the minimum limit. (b) Enlarged view of the faulted crater (unnamed) showing the area
828 chosen for the counting (outlined in blue) and the counted craters. In red are the primary craters considered
829 for the count, in yellow the secondaries which were excluded from the count. (c) Enlarged view of Kyosai
830 crater. The count was performed on a NAC image (EN0220675399M; 65 m/pixel). Symbology as in (b). The
831 crater SFDs of the system (black squares), of the faulted crater (red filled circles), and of Kyosai crater
832 (green filled stars) were plotted and compared with LWPF porous scaling law (d), and NPF (e) to obtain the
833 absolute model age for the system.

834 Fig.8 Al-Hamadhani thrust system, named after Al-Hamadhani crater (a). (b) Structures encompassed in the
835 system (in red; triangles indicate the dip direction of the thrust), verge toward NW. Opposite vergence was
836 observed in correspondence of four craters (indicated by white arrows; see text for more details). On the
837 background is a MDIS high solar incidence angle BDR mosaics (on the left: HIWmosaic; on the right: HIE
838 mosaic; the grey stripe in the center of the image is due to the different illumination conditions of the images
839 used for the mosaics) (166 m/pixel) in equirectangular projection.

840 Fig.9 Dating Al-Hamadhani thrust system. (a) Buffer areas (in green) created around lineaments (outlined in
841 red). Craters overlapping the structures and considered for the counting are outlined in blue. The faulted and
842 the unfaulted craters are indicated by a pink and a white arrow, respectively. (b) Enlarged view of the faulted
843 crater (unnamed) showing the area chosen for the counting (outlined in blue) and the counted craters (in red).
844 (c) Enlarged view of the unfaulted crater (unnamed). The count was performed on a NAC image
845 (EN0211416032M; 100 m/pixel). Symbology as in (b). The crater SFDs of the system (black squares), of the
846 faulted crater (red filled circles), and unfaulted crater (green filled stars) were plotted and compared with
847 LWPF porous scaling law (d), and NPF (e) to obtain the absolute model age for the system.

848 Fig.10 Enterprise system named after Enterprise rupes (a). (b) The system's structures, outlined in red
849 (triangles indicate the dip direction of the thrust), verge toward SE (see text for more details). On the
850 background is a MDIS high solar incidence angle BDR mosaic (166 m/pixel) in equirectangular projection.

851 Fig.11 Dating Enterprise thrust system. (a) Buffer areas (in green) created around lineaments (outlined in
852 red). Craters overlapping the structures and considered for the counting are outlined in blue. White arrow
853 indicates the unfaulted crater chosen for the minimum system's age limit estimation. (b) Rembrandt basin
854 was chosen for the maximum age limit. The area considered for the count is outlined in blue. In red are the
855 primary craters considered for the count, in yellow the secondaries, excluded from the count. (c) Enlarged
856 view of the unfaulted crater (unnamed). The count was performed on a NAC image (EN1059205122M; 49
857 m/pixel). The crater SFDs of the system (black squares), of the Rembrandt basin (red filled circles), and
858 unfaulted crater (green filled stars) were plotted and compared with LWPF porous scaling law (d), and NPF
859 (e) to obtain the absolute model age for the system. The steepening observed in the NPF chart for the smaller
860 craters can be due to the presence of possible secondary craters since the counted area includes the basin
861 proximal ejecta, where secondaries could be formed during the impact that formed the basin itself.

862

863

864

865

866

867

868

869

870

871

872

873

874

875

876

877

878

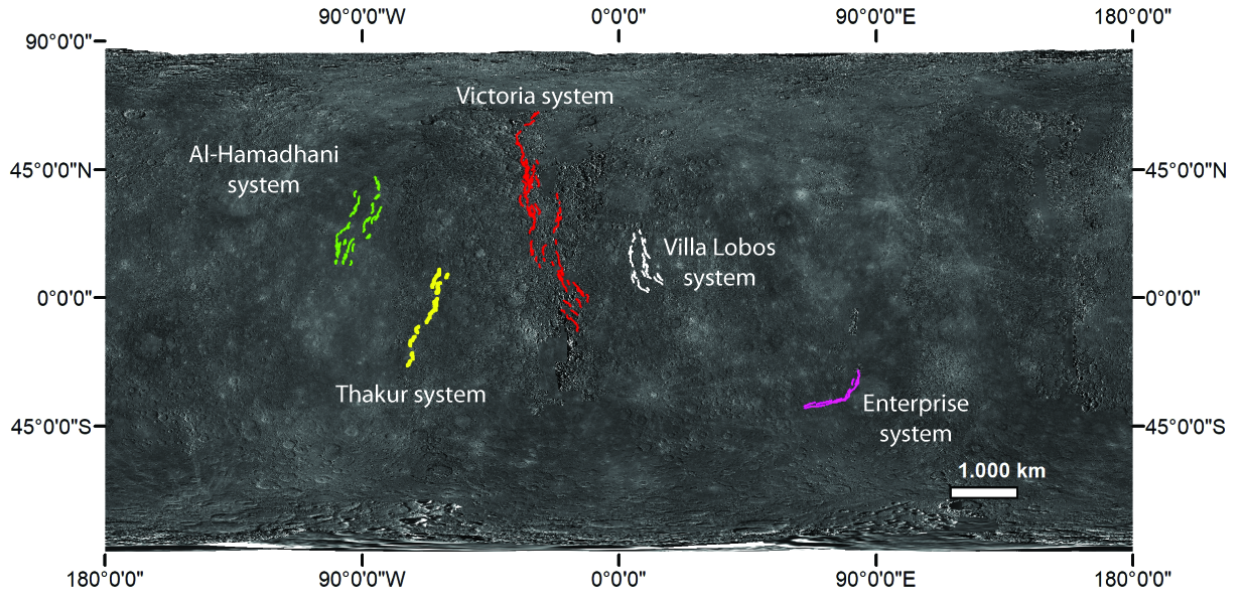
879

880

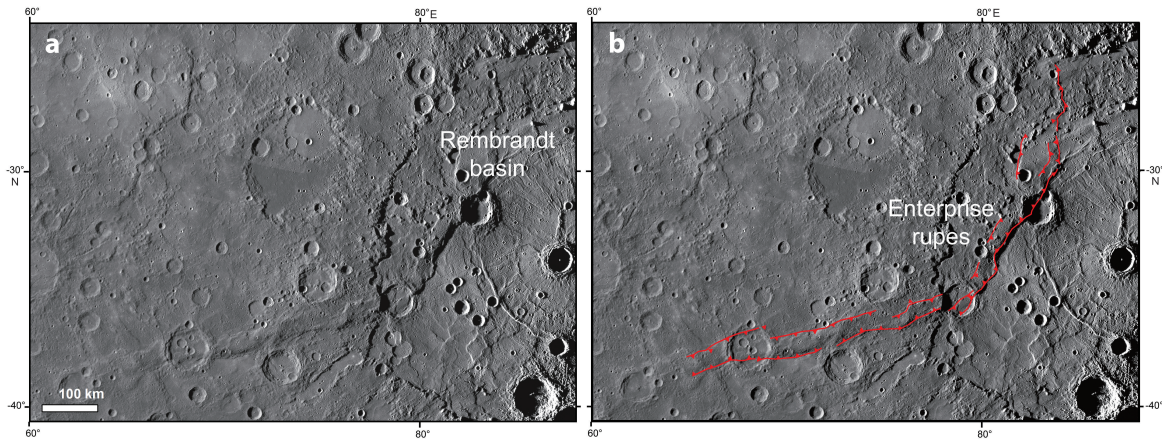
Table 1 Model ages and maximum and minimum age limits of the five thrust systems investigated in this work

	LWPF (porous scaling law)	LWPF (non-porous scaling law)	NPF
Thakur system:	3.7 (+0.03/−0.06) Ga	990 (±300) Ma	3.6 (+0.04/−0.06) Ga
Maximum age limit (Thakur crater)	3.7 (+0.01/−0.02) Ga	150 (±10) Ma	3.8 (±0.02) Ga
Minimum age limit	84 (±20) Ma	2.6 (±0.5) Ma	260 (±60) Ma
Victoria system:	3.7 (+0.02/−0.02) Ga	1.0 (±0.2) Ga	3.8 (±0.02) Ga
Maximum age limit (Donne crater)	3.8 (+0.01-0.02) Ga	300 (±40) Ma	3.9 (±0.02) Ga
Minimum age limit	2.4 (±0.4) Ga	49 (±9) Ma	3.5 (+0.05/−0.08) Ga
Villa Lobos system:	3.6 (+0.09/−0.8) Ga	720 (±300) Ma	3.6 (+0.06/−0.01) Ga
Maximum age limit	3.7 (+0.02/−0.03) Ga	990 (±300) Ma	3.9 (+0.04/−0.05) Ga
Minimum age limit (Kyosai crater)	1.3 (±0.4) Ga	32 (±9) Ma	3.4 (+0.1/−0.5) Ga
Al Hamadhani system:	3.7 (+0.02/−0.03) Ga	970 (±200) Ma	3.8 (±0.03) Ga
Maximum age limit	3.8 (+0.01/−0.02) Ga	760 (±200) Ma	3.9 (+0.02/−0.03) Ga
Minimum age limit	100 (±40) Ma	2.1 (±0.7) Ma	300 (±100) Ma
Enterprise system:	3.7 (+0.03/−0.04) Ga	2.1 (±0.7) Ga	3.8 (+0.05/−0.08) Ga
Maximum age (Rembrandt basin)	3.8 (±0.007) Ga	3.1 (±0.3) Ga	3.85 (±0.1) Ga (from Ferrari et al.,2015)
Minimum age	950 (±200) Ma	27 (±7) Ma	2.0 (±0.4) Ga

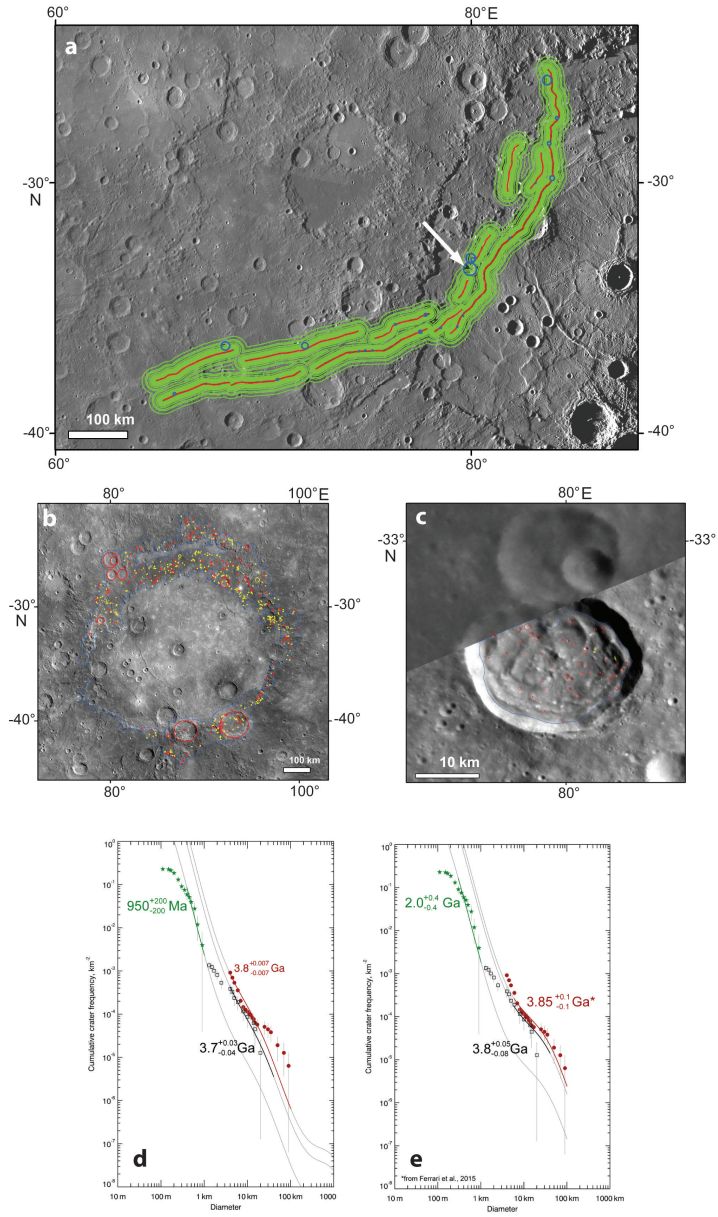
Thrust systems and craters have been dated using both Le Feuvre and Wieczorek Production function (LWPF) and Neukum Production Function (NPF). For LWPF both porous and non-porous scaling law results have been reported, although just the formers have been considered in this work (see text for more details).

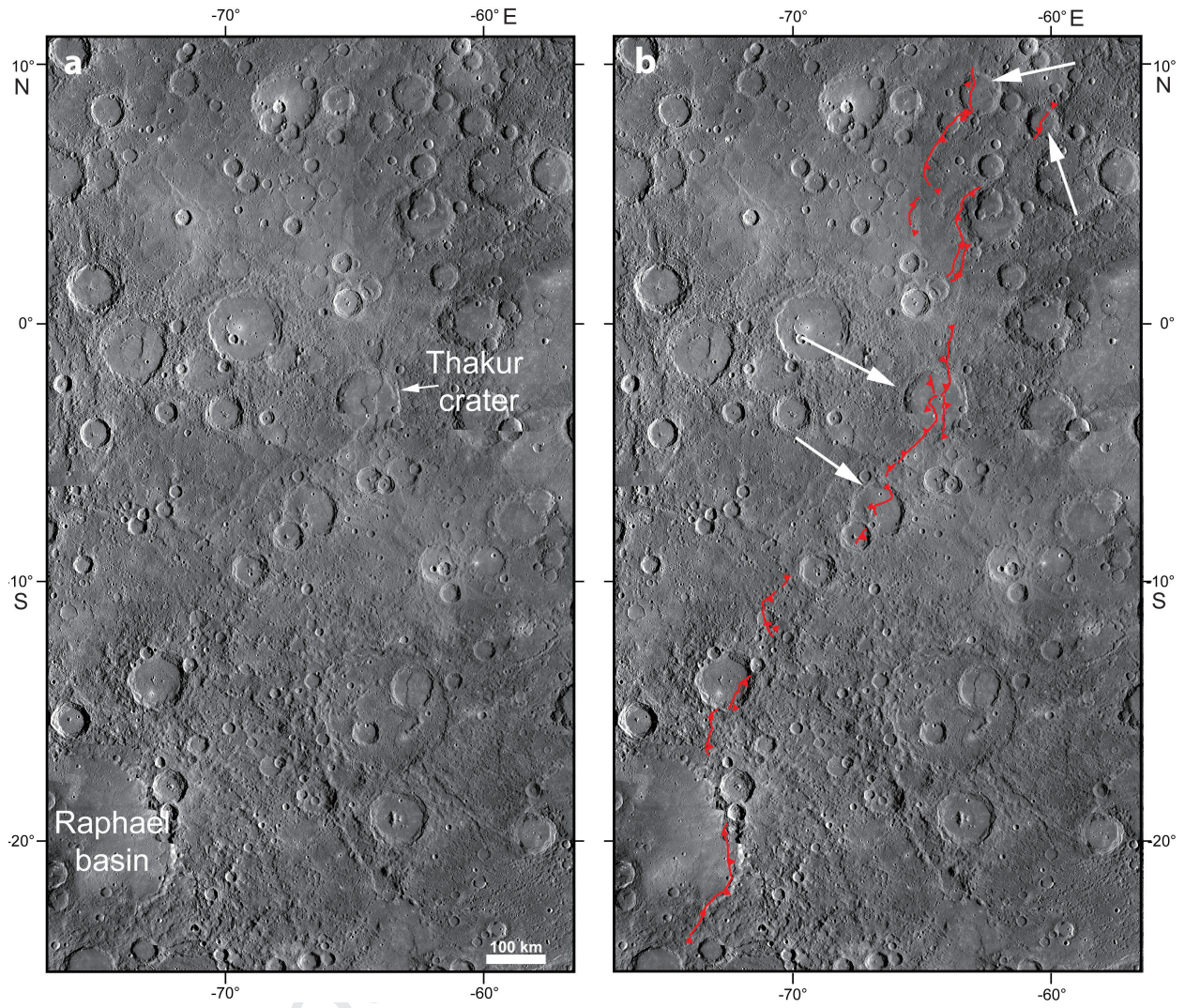


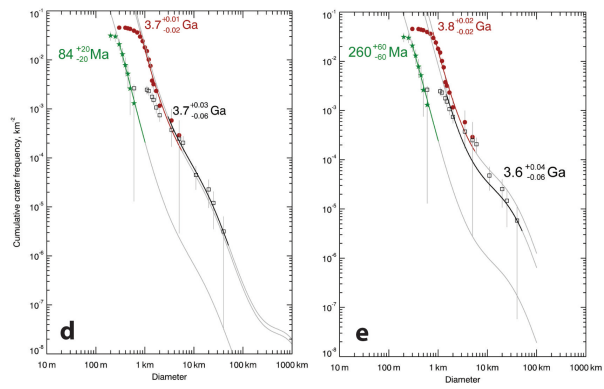
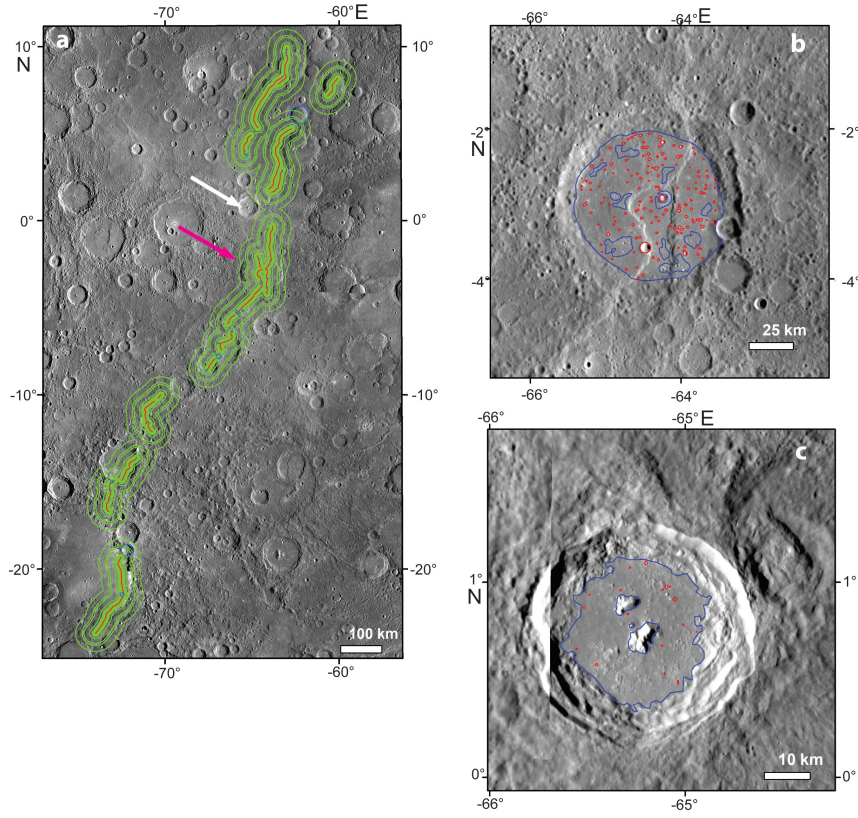
Journal Pre-proof

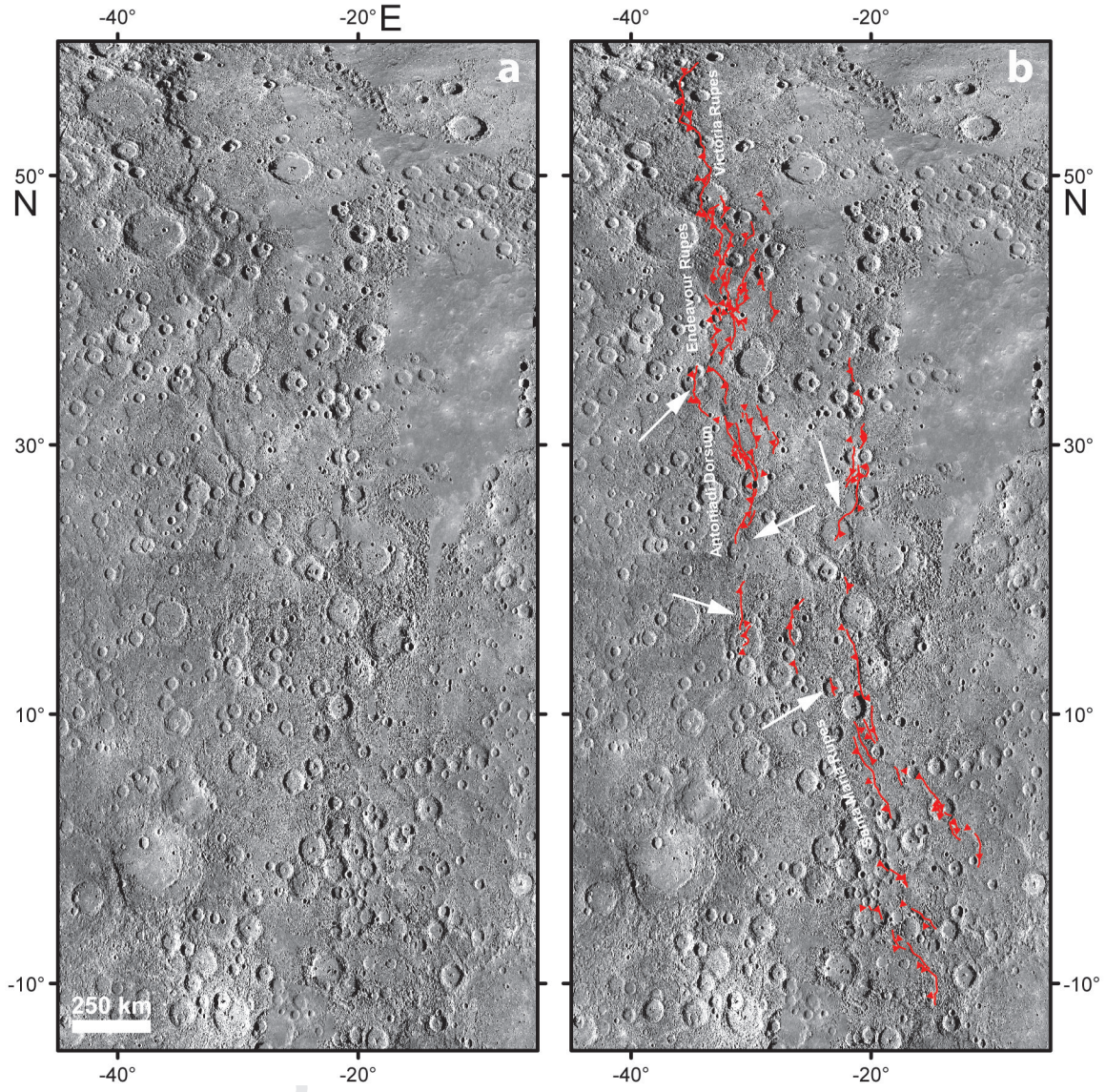


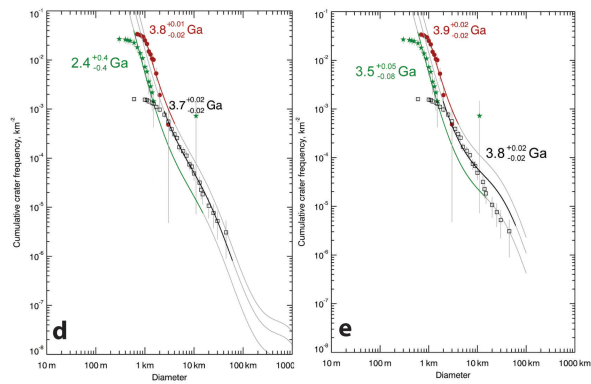
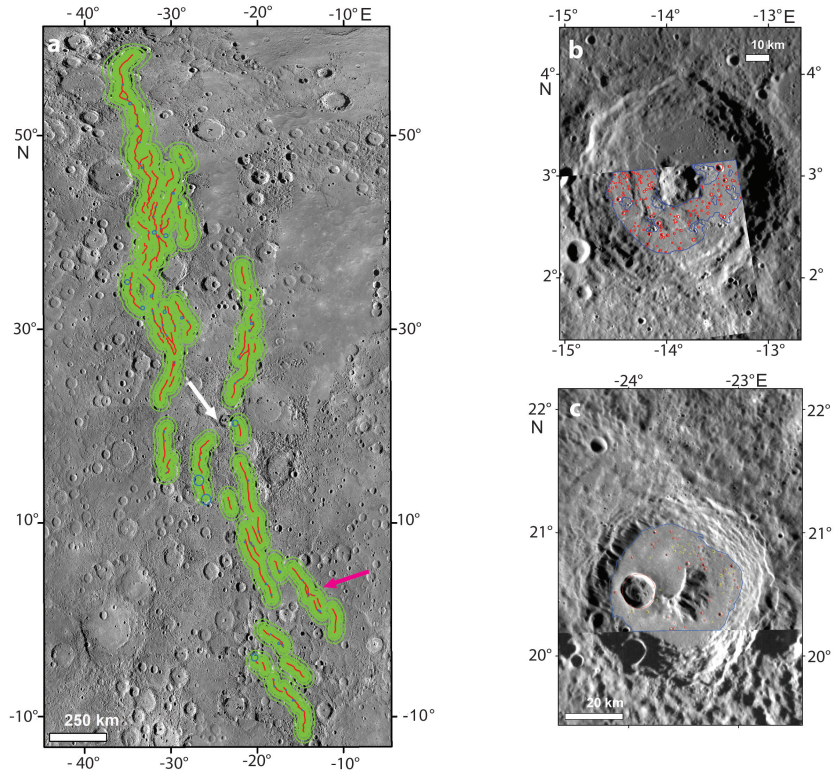
Journal Pre-proof

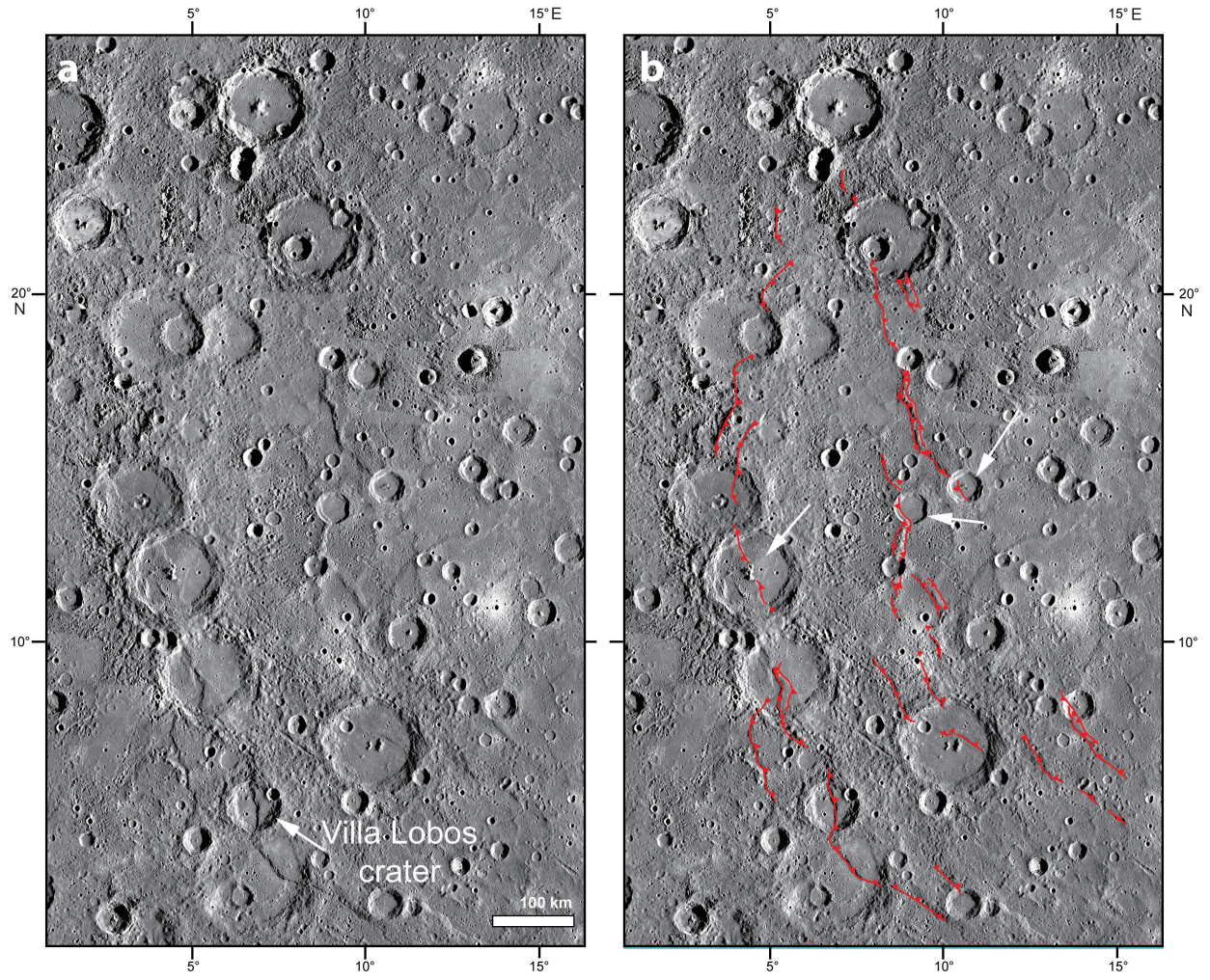


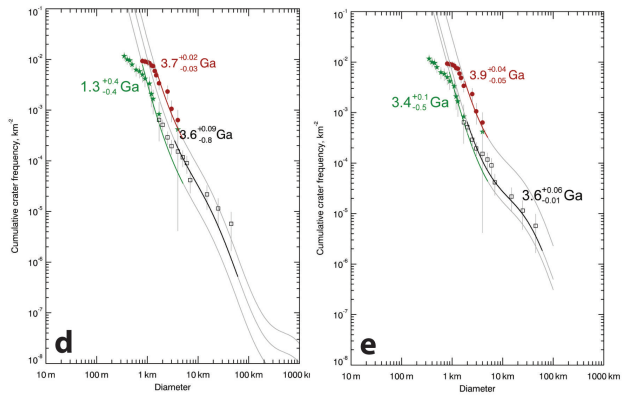
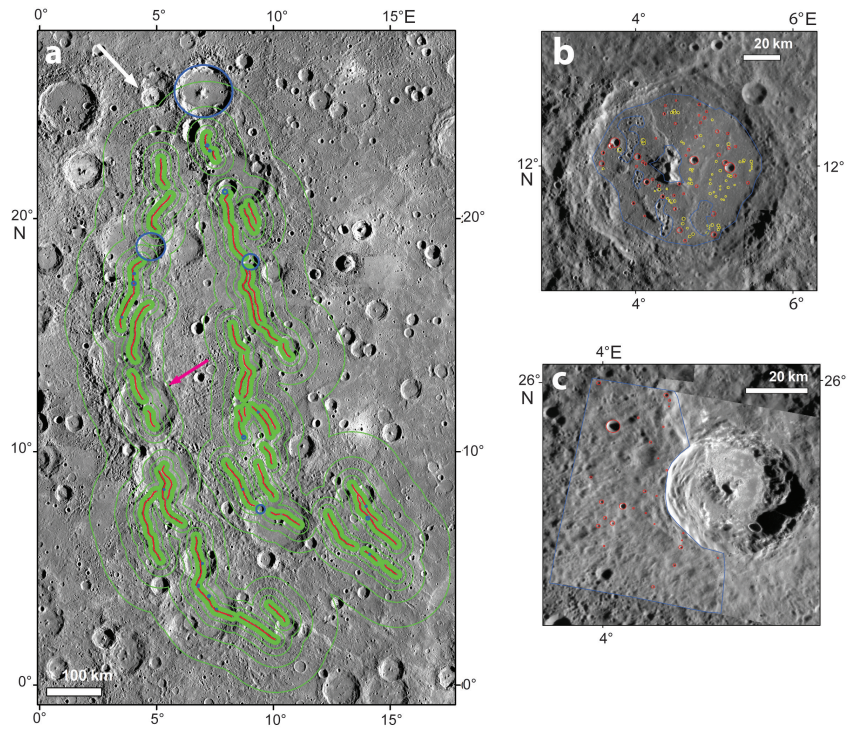


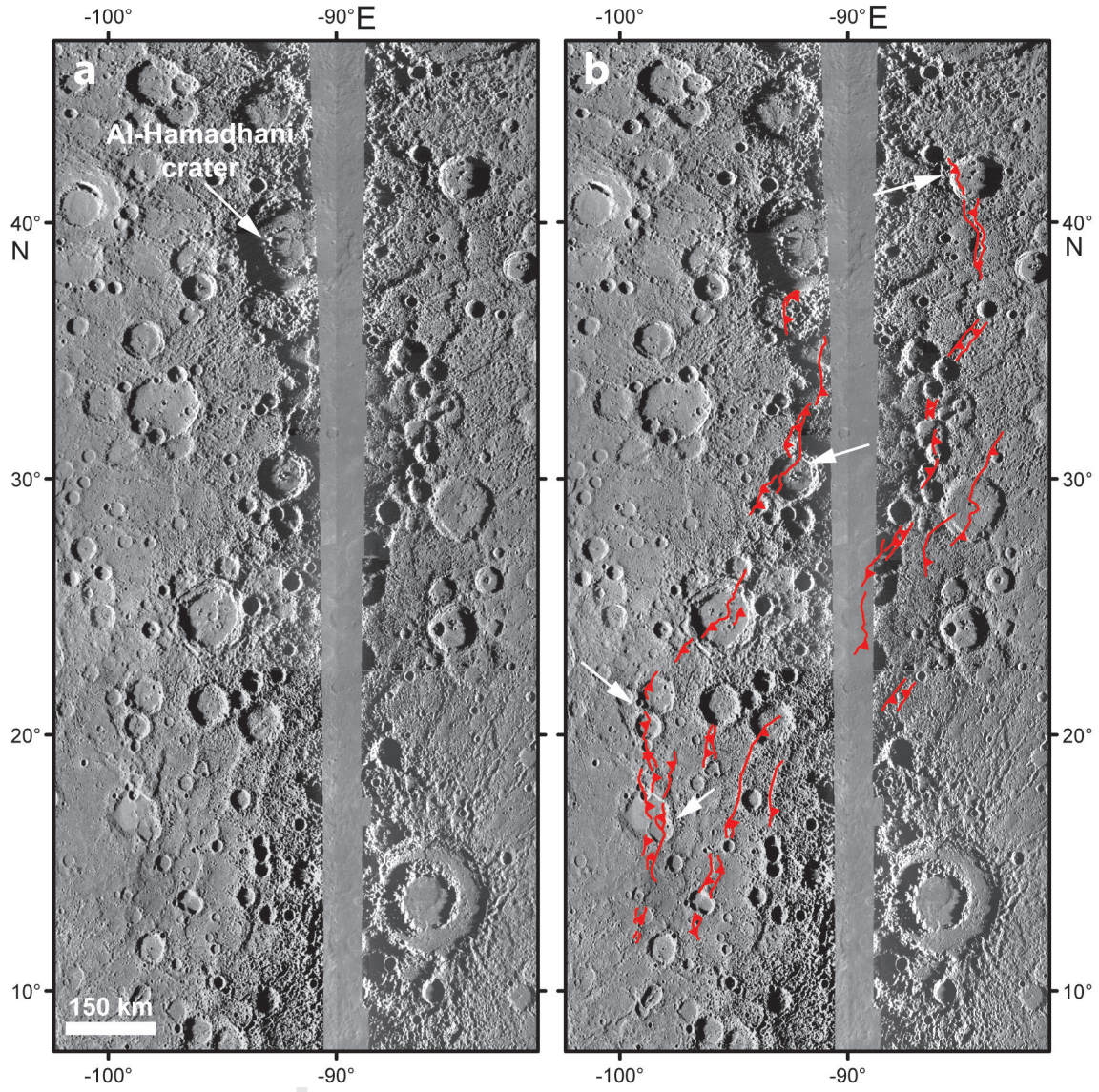


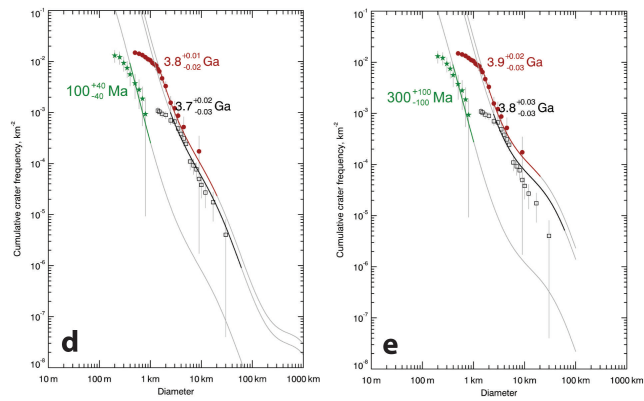
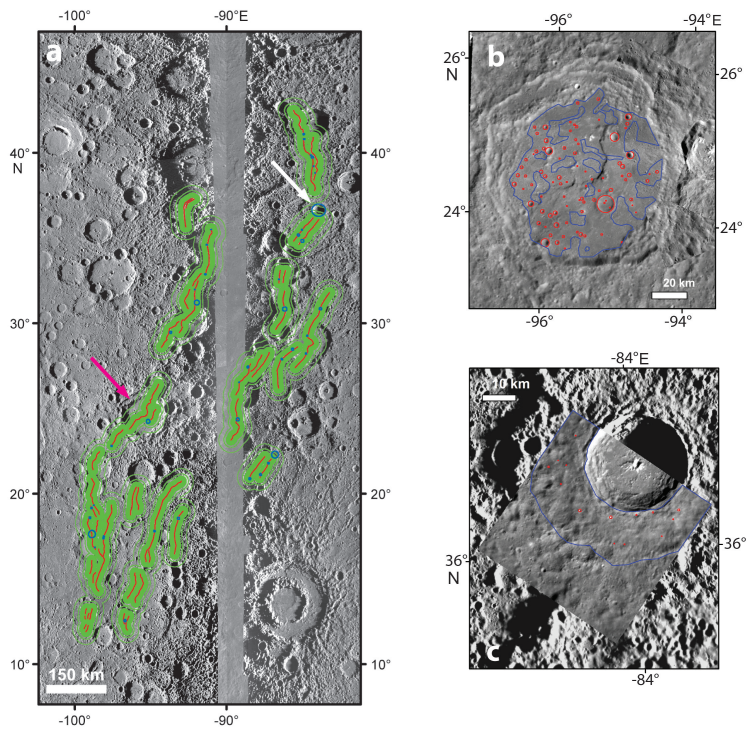












- Activity along thrust systems all over Mercury has most likely ended at about 3.6-3.7 Ga
- Dating thrust systems gave new clues to better understanding the thermal evolution of the planet
- Tidal despinning and/or mantle convection may have contributed to Mercury evolution

Journal Pre-proof

Declaration of Interest Statement

Journal Pre-proof